Cell Reports
Physical Science

CellPress
OPEN ACCESS

Article

High-throughput assessment of two-dimensional electrode materials for energy storage devices

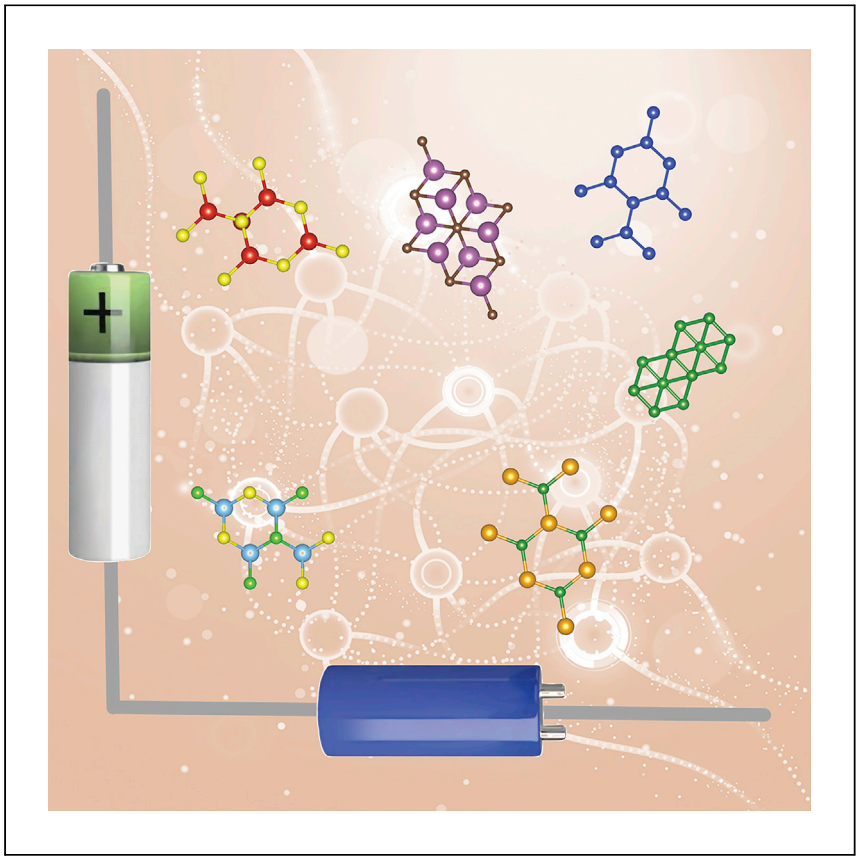

2D materials are ideal candidates for energy storage at nanoscale. Kabiraj and Mahapatra present an automated computational pipeline for identifying potential contenders from massive 2D material space. The uniqueness of the approach lies in defining appropriate descriptors to simplify a computationally hard problem. The informatics may pave the way for next-generation hybrid energy storage systems.

Arnab Kabiraj, Santanu Mahapatra

santanu@iisc.ac.in

Highlights

High-throughput computational pipeline to scan massive material space

Machine learning model to assist rapid discovery

Descriptor-based guidelines to identify materials for high Li-ion storage

Curated materials satisfy requirements for both supercapacitor and Li-ion battery

Kabiraj & Mahapatra, Cell Reports Physical Science *3*, 100718
January 19, 2022
https://doi.org/10.1016/j.xcrp.2021.100718

Cell Reports
Physical Science

CellPress
OPEN ACCESS

Article

High-throughput assessment of two-dimensional electrode materials for energy storage devices

Arnab Kabiraj[1,2] and Santanu Mahapatra[1,3,4,*]

SUMMARY

The ultra-large surface-to-mass ratio of two-dimensional (2D) materials has made them an ideal choice for electrodes of compact lithium (Li)-ion batteries and supercapacitors; however, only a small fraction of the massive 2D material space has been investigated for such applications. Here, combining explicit-ion and implicit-solvent formalisms, we develop an automated, first-principles-based, high-throughput computational framework to assess thousands of such materials. We define four descriptors to map "computationally soft" single-Li-ion adsorption to "computationally hard" multiple-Li-ion-adsorbed configuration located at global minima for insight finding and rapid screening. Leveraging this large dataset, we also develop crystal-graph-based machine learning models for the accelerated discovery of potential candidates. A reactivity test with commercial electrolytes is further performed for wet experiments. Our holistic approach, which predicts both Li-ion storage and supercapacitive properties and hence identifies various important electrode materials that are common to both devices, may pave the way for next-generation energy storage systems.

INTRODUCTION

With the rapid emergence of electric vehicles in recent times, there is demand for providing sustainable, economically viable, and lightweight energy storage systems.[1] The immediate solution so far has been the lithium (Li)-ion battery (LIB)[2], but supercapacitors and supercapacitor-battery hybrid systems have been proposed as a viable long-term alternative. This recognition arises since these systems have sizable power density; long cycle life; extremely fast charging/discharging speed; high input/output current capability; simple charging and discharging circuits; decent low/high-temperature operations; and most importantly, small size, low weight, and low cost.[3] In the quest for lighter and smaller energy storage devices, electrode materials with high surface-to-volume and surface-to-mass ratios (high specific areas) are highly desired for both batteries and supercapacitors. Since the successful exfoliation of graphene,[4] two-dimensional (2D) materials have attracted tremendous interest in this field.[5–7] However, most research efforts, both computational and experimental, have been directed toward LIBs.[8–10] Experimental research on 2D materials-based supercapacitors has escalated in the recent past,[11,12] but computational studies of these materials as supercapacitor electrodes have been scarce. The extensive treatment of the electrolyte and requirement of grand canonical calculations to simulate the applied voltage makes these studies extremely challenging.[13,14] However, significant strides in these domains have been made recently,[15–21] resulting in tools such as joint density-functional theory (JDFT)[22] that allow accurate calculation of the electrochemical properties of any solid surfaces using an implicit and continuum solvation model. Recently, this tool

[1]Nano-Scale Device Research Laboratory, Department of Electronic Systems Engineering, Indian Institute of Science (IISc), Bengaluru 560012, India

[2]Twitter: @arnabkabirajeng

[3]Twitter: @santanu80999226

[4]Lead contact

*Correspondence: santanu@iisc.ac.in

https://doi.org/10.1016/j.xcrp.2021.100718

has been used successfully to analyze the phenomenon of under-potential deposition (UPD) of Cu on Pt[111] surface[14] and to accurately predict supercapacitive performances of Ag[100] surface,[20,21] graphene, and various borophene phases.[23–25] Similarly, the introduction of new techniques such as global minima searching for determining cation storage capacities of 2D materials, such as MoS_2, ReS_2, and VS_2, have resulted in much more realistic predictions, albeit at the cost of a high computational budget.[26–28]

At the same time, recent advances in computational methodologies have also spurred several high-throughput computational studies, resulting in many generic 2D material databases that contain both synthesized and theoretically predicted materials.[29–35] Several first-principles-based studies have focused on these databases to find exceptional application-specific 2D materials, such as materials with nontrivial topological order,[36] high-temperature ferromagnetism,[37] excellent catalytic activity for hydrogen evolution,[38] water-splitting photocatalysis,[39] and exotic charge density wave (CDW) properties.[40] However, due to the computation challenges, the prediction of energy storage capacity of these materials has not yet been attempted by any high-throughput study; hence, the enormous 2D material space has remained mostly unexplored.

In this work, based on explicit-ion and implicit-solvent formalisms, we develop a high-throughput computational framework to assess thousands of 2D electrode materials for LIB and supercapacitors. From the DFT-calculated single-Li (SL)-binding properties of a material, we devise *four* descriptors to estimate its maximum Li-ion storage capacity. After analyzing a total of 1,941 materials from a database (Computational 2D Materials Database or C2DB),[34,35] we define precise ranges of these descriptors, translating to a high specific capacity. Such descriptors-based mapping from simple SL-ion to complex multi-Li-ion adsorption is validated using the rigorous global-minima-searching technique. We then use a series of JDFT calculations (i.e., DFT combined with implicit solvent and fixed-potential grand canonical) to estimate the supercapacitive performance of 3,691 materials from the same database. This massive computational result is then used to develop crystal-graph-based machine learning (ML) models for accelerated prediction of the descriptors for Li-ion storage and the specific capacitance. We find several potential materials from other databases using the ML models. We also examine the reactivity of these materials against commercial electrolytes using DFT calculations. Our all-inclusive computational approach, which discovers several potential electrode materials for both LIB and supercapacitors, may pave the way for the practical application of 2D material-based energy storage systems.

RESULTS

Overview of high-throughput computational framework

The computational framework developed in this work is outlined in Figure 1. Among many available 2D materials databases,[29–35] we begin our study with C2DB. The materials of C2DB have been explored by a "systematic combinatorial approach" where almost all known layered exfoliable materials are covered,[29] and by substituting different species, a host of new materials were predicted. The latest version of C2DB[35] also contains various alloyed 2D materials. This kind of variation is ideal for training ML models, which is one of our primary goals. Also, recent synthesis of species-substituted 2D materials[41] and solid solutions[42,43] with no bulk analogs has made practical applications of this kind of "synthetic" 2D materials possible. C2DB contains several material properties of interest, including bandgap,

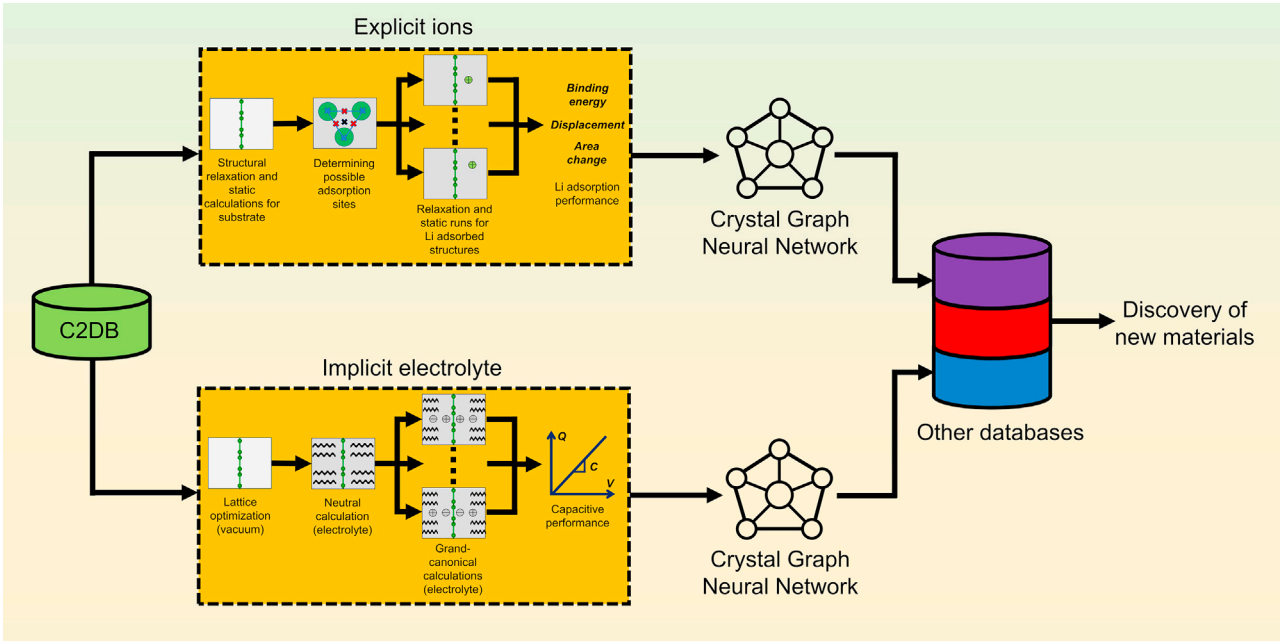

Figure 1. Schematic of the high-throughput workflow combining DFT and ML

thermodynamic stability, and energy above the convex hull, which helps us estimate the usefulness and the chance of potential synthesis of these materials. After some initial screening (discussed later), the figure of merits (FOMs) of around 2,000 materials are calculated for Li-ion storage application, while the FOMs of more than 3,500 materials are calculated for supercapacitor electrode application. The computational cost for examining the suitability of a material as a supercapacitor anode is far less than that of examining the same material's merit as a LIB electrode. In the former case, a reasonable implicit electrolyte model is assumed, while the latter examination requires dealing with explicit Li-ion and several lattice optimizations. The crystal structure to FOM mapping is then learned using a state-of-the-art crystal graph neural network. With reasonable accuracy, these ML models are then used to rapidly screen new materials from other 2D materials databases, and ultimately the ML predictions are verified using rigorous (J)DFT-based methodology. This enables the discovery of new and interesting materials at an accelerated pace.

Choice of the descriptors for Li-ion adsorption

The ultimate FOM for materials as LIB electrodes is the specific capacity, which indicates how much charge the material can store per unit mass via Li-ion adsorption. The other two important FOMs are the average open circuit voltage that ultimately decides the cell voltage and the activation energies for the diffusion of the Li-ion that indicates how fast the material can be charged.[28,44] The activation energy estimations involve extremely rigorous and equally expensive nudge elastic band (NEB) calculations for every possible Li-ion diffusion path, which simply cannot be done in a high-throughput manner. We therefore focus solely on the Li-ion storage capacity of the materials in this work. The average open circuit voltage with the maximum amount of adsorbed Li-ion can simply be estimated as the absolute value of the binding energy per Li-ion. These quantities are calculated from the following equations:[28]

$$BE = \frac{E_{\mathrm{mat+Li}} - E_{\mathrm{mat}} - n\mu_{\mathrm{Li}}}{n}\ [\mathrm{eV}] \qquad \text{(Equation 1)}$$

$$OCV \approx \mathrm{abs}\left(\frac{\left[E_{\mathrm{Li}_{x_{max}}\mathrm{mat}} - E_{\mathrm{Li}_{x_{min}}\mathrm{mat}} - (x_{max} - x_{min})\mu_{\mathrm{Li}}\right]}{(x_{max} - x_{min})e}\right)[\mathrm{V}] \qquad \text{(Equation 2)}$$

where BE signifies the average binding energy per Li-ion, E_{mat+Li} is the energy of n number of Li-ion-adsorbed 2D material system, E_{mat} is the energy of monolayer substrate, μ_{Li} is the chemical potential (cohesive energy per atom) of bulk Li, OCV is the average open-circuit voltage of maximum number of Li-adsorbed 2D material, x_{min} = 0 is the amount of Li per formula unit of 2D material in initial pristine form, x_{max} is the maximum amount of Li per formula unit the material can store, and e is the electronic charge. Clearly, OCV equals to the absolute value of BE with these definitions. Note that when the material is being examined as an anode, a low value of OCV is desired to maximize the cell voltage. However, if the material is viewed as a prospective cathode, the converse is required.

In addition to these quantities, the specific capacity (SC) of a material is determined from the following equation:

$$SC = \frac{1}{MW_{mat}}\left(x_{max} v F.10^3\right)[\mathrm{mAh/g}] \qquad \text{(Equation 3)}$$

where MW_{mat} is the molecular weight of the material, F = 26.801 Ah/mol is the Faraday's constant, and v = 1 is the number of valence electrons for Li.

There have already been a plethora of first-principles-based studies to examine the suitability of various 2D materials as LIB electrodes[10,45] using the "uniform adsorption" model. This is the probable reason that the computed specific capacities are usually vastly overestimated compared with the experimental findings.[44,46] Rigorous global-minima-searching-based computational studies have highlighted the limitations of the "uniform-adsorption" model, while predicting the most stable cation-adsorbed phase and the corresponding specific capacity for 2D materials.[26–28] Moreover, the conventional model-based studies cannot incorporate the non-ideal effects of multiple charging-discharging cycles, such as bond breaking and formation, the phase change of adsorbent, irreversible Li adsorption, electroplating, and so on. In such cases, the uniform-adsorption-predicted theoretical specific capacity might match the experimental values for the first few cycles, but rapid capacity fading soon reduces the quantity to a much lower reversible "effective capacity."[28,47] All of these studies indicate that a structure-searching procedure must be used to determine the realistic Li storage capacity of a 2D material. These procedures are extremely expensive computationally as they often involve hundreds of large-supercell lattice optimizations for a single material and therefore are unsuitable for examining thousands of materials in a high-throughput manner. However, the study of adsorption of a single Li-ion in a 2D material is much more straightforward, computationally cheaper, and requires only a few tens of lattice optimizations or ionic relaxations at most. In this work, we observe how different 2D materials behave when a single Li-ion gets absorbed in them, and from the adsorbed relaxed structures, we obtain suitable relevant descriptors that help us in extrapolating how the material would behave when storing a "full-house" of Li-ions. At maximum adsorbed concentration, to minimize the system energy, usually, all the Li-ions are held at the most stable binding site, which can easily be determined from SL adsorption studies. However, any material can have multiple binding sites, and ideally, these sites should be discovered with suitable random structure searching, especially if the material lacks symmetry.[28,48] Nevertheless, if the material is symmetric, the possible binding sites can be identified from manual inspection, as the binding

sites are usually located either "on top" of the surface atoms or at the "hollow" or "bridge" sites. Based on this intuition, an algorithm was recently developed that can triangulate and enumerate the possible binding sites for any surface, which has been carefully verified and subsequently refined with experimental results in terms of binding energies, also called adsorption energies.[49] Based on this algorithm, we develop a fully automated high-throughput code that places a single Li-ion on these possible binding sites of any 2D material and finds the most stable SL-adsorbed structure via DFT-based atomic relaxations and energy calculations. Next, we take note of 4 crucial properties as metrices to predict how they would perform when stored with a "full-house" of Li cations.

The first and probably the most important descriptor is the binding energy (BE_{SL}), which is a direct indicator of average binding energy (BE_{max}) with the maximum amount of Li adsorbed. With more Li-ion stored, the electrostatic repulsion between the ions becomes effective, and the value of binding energy keeps increasing.[28] However, there are exceptions where BE_{max} can become even less than BE_{SL} with severe structural changes in some unusual cases.[28,50] As per the definition, more negative binding energy indicates tighter Li binding, while a positive value indicates the possibility of Li clustering and phase separation with the substrate. However, too negative BE_{SL} can be a problem as this indicates electron deficiency and thus instability of the material in the pristine and freestanding form. This also points to extremely tight Li binding that could lead to bond cleavage in the material or an amorphous phase with a higher amount of Li stored. Also, as discussed before, the absolute value of the BE_{max} quantifies the average *OCV*, and for materials viewed as a prospective anode, which is the case most of the time, this should be as small as possible in magnitude. The ideal BE_{SL} should therefore be a moderately negative quantity.

Our second and third descriptors tell us about the mechanical sturdiness of the material after a single Li-ion is adsorbed at the most stable site. These are the rms displacement ($disp_{rms\text{-}SL}$) of all the atoms of the substrate per area (before Li adsorption) and the percentage of area change (ΔA_{SL}) after Li adsorption. Clearly, the lower the absolute value of $disp_{rms\text{-}SL}$ or ΔA_{SL}, the greater chance the material would have of retaining its structural integrity with a "full-house" of Li-ions stored. Also, a drastically high magnitude of either of these two descriptors indicates a possibility of phase change upon lithiation, which is somewhat common with 2D materials but mostly undesired in LIB applications.[26,28,47]

The fourth descriptor, the simplest one, is the amount of charge transfer (q) from the adsorbed Li to the substrate. Ideally, this should be $-1e$. However, with different kinds of complex interactions, this value can range from mildly positive to even less than $-1e$. This value has to be as negative as possible to have a high specific capacity. However, high negative values can also indicate a strong reaction between the Li and the substrate, which is undesirable.

Using 2H-MoS_2 as a prototype, we have described the procedure of identifying the most stable SL binding site and the number of unique binding sites in Figure 2A. In Figure 2B, we illustrate the concept of $disp_{rms\text{-}SL}$ by superimposing the structures of the pristine material, and the material with a Li adsorbed at the "Top Mo" site, which is highlighted with a red dotted circle.

Initial screening for LIB electrode materials

The important intrinsic properties for a material to be considered as LIB electrodes are low or preferably zero bandgaps for high charge conductivity and high specific

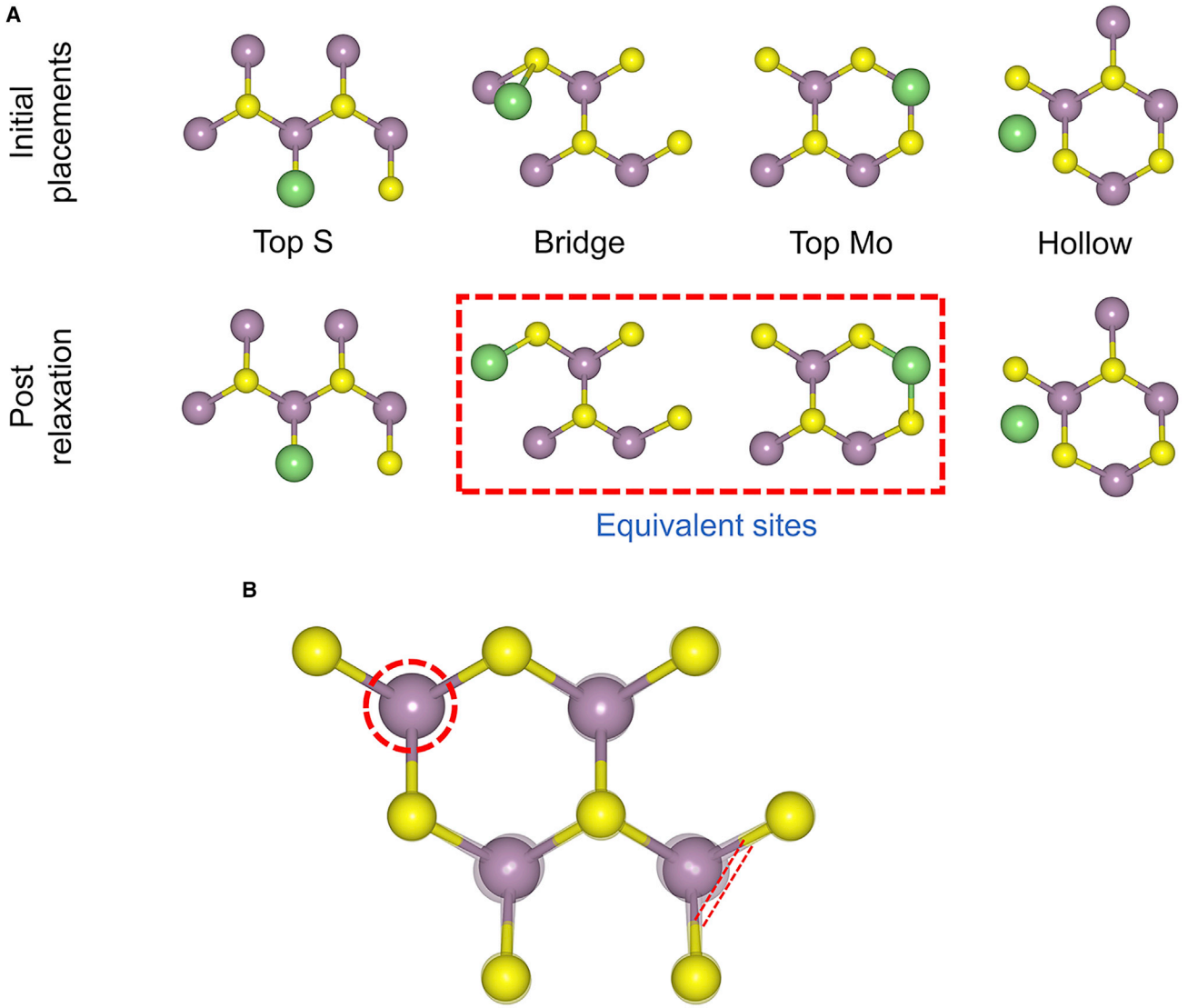

Figure 2. Identifying binding sites and defining atomic displacement

(A) The algorithm finds four unique adsorption sites: the top of the S atom, the bridge between Mo and S atoms, the top of the Mo atom, and the hollow space at the center of the Mo-S hexagon. After lattice optimizations, the Li placed at the bridge site moves to the top of the nearest Mo, indicating theirs is no stable bridge site in MoS_2. A symmetry-based analysis is then performed on all four relaxed structures, where the equivalence between relaxed Bridge and Top Mo sites are established, reducing the number of unique adsorption sites to 3. The most stable site turns out to be the Top Mo site with BE_{SL} = −0.5 eV, $disp_{rms\text{-}SL}$ = 0.59/Å, ΔA_{SL} = 1.87%, and q = −0.85 e.

(B) Assuming the most stable adsorption site as a reference, the displacement after Li adsorption of the Mo atom at the bottom right is quantified by the distance between the two parallel red lines. The displacement of all atoms can be calculated similarly, the root mean square of which is then taken and normalized by the cell area before adsorption to obtain the quantity $disp_{rms\text{-}SL}$. The purple, yellow, and green balls represent Mo, S, and Li atoms, respectively.

area ($A_{specific}$), i.e., high effective surface area of the material per unit of mass. In addition, the materials should be dynamically and thermodynamically stable for their experimental realization. In the current version of C2DB, there are 423 materials exhibiting zero Perdew-Burke-Ernzenhof (PBE) bandgap and high dynamic and thermodynamic stabilities. This number is probably too small to train a reliable ML model. However, there are real materials that pose apparent exceptions to the above-stated screening criteria. For instance, silicene is classified as a material with low thermodynamic stability in C2DB, but silicene transistors have been

demonstrated to work at room temperature.[51] Many commonly used 2D materials, such as T-phase MoS_2 showing dynamic instability[52] in freestanding form, stabilize themselves on substrates through possible substrate interaction and even find application in room-temperature devices.[53] Also, these materials can show CDW characteristics and stabilize in a larger supercell with slight structural distortion.[40] On the other hand, despite showing a sizable bandgap, ReS_2 has been experimentally demonstrated to be a high-current-density decent LIB anode material.[54] Hence, we also include around 1,500 more randomly selected materials in our dataset that show PBE bandgap up to 1 eV and are classified to have low, medium, or high thermodynamic and dynamic stabilities. Considering the cost of the DFT calculations, this number is deemed large enough to reliably train deep-learning-based ML models. We exclude all the janus materials as our methodology is not equipped to handle the inhomogeneous surface terminations.

Data analysis and ML for single Li-ion adsorption

After performing all the DFT-based relaxations and energy calculations, we end up with a total of 1,941 data points (Data S1). The data are summarized in Figure 3, where the above-mentioned four SL-ion descriptors are plotted against the most important intrinsic property of the material, the specific area. The histogram distribution of these quantities is shown in Figure S1. Note that to have an excellent specific capacity, a material should have values in the desired range for all four descriptors, while maintaining a decently high value of $A_{specific} > 750$ m^2/g. Analysis of the data with random structure searching/delithiation (narrated in detail in the following section), and manual visualization for some selected structures reveal that the "sweet spot" for BE_{SL} is in the range -0.4 to -2.0 eV. As discussed before, the values of $disp_{rms\text{-}SL}$ and ΔA_{SL} for a good Li-storing material should be nearly zero, and we find the desired absolute values here to be lower than 1/Å and 1%, respectively. The value of q_{SL} can be as negative as -1.6 e for some materials, but the structural integrity of these materials is questionable even with a single Li adsorbed. Most materials show q close to -0.8 e, indicating transfer of almost one electron to the substrate and formation of Li^+ ions, just as intended for LIB systems. We define this range as -0.55 e to -1 e. We shortlist a total of 10 materials, which has all four descriptor values in the desired range with a decent $A_{specific}$. These points are highlighted in Figure 3. Among these, silicene (Si2_A-164-d) shows the highest $A_{specific}$ = 2,777 m^2/g, but has already been well established as an excellent Li storage material in our previous structure-searching-based study.[47] The second material with $A_{specific}$ = 2,569 m^2/g is boron phosphide (BP_AB-187-df), which has also been established as an excellent LIB anode material by a previous study.[50] There are four materials with $A_{specific}$ values 832–1,114 m^2/g that belong to the 2-layer bare MXene category with the formula M_2X, where M = Sc/Ti and X = C/N. Again, numerous conventional "uniform-adsorption" first-principles-based studies have established these materials as excellent LIB anodes.[55–59] However, none of these studies have implemented the gold standard of global minima searching to examine the materials' suitability as electrodes, and neither have checked the materials for reactivity with the electrolytes. We proceed with some of these for further stringent evaluations.

Because of an ever-increasing amount of available data, ML has recently found many applications in the field of solid-state materials science.[60–62] Among many models, graph-based neural networks have received special attention since they do not require complex transformations to generate feature vectors and can accurately predict diverse physical properties directly from the crystal structures with a moderate amount of data.[63–66] After rigorous testing (see Experimental procedures), we select

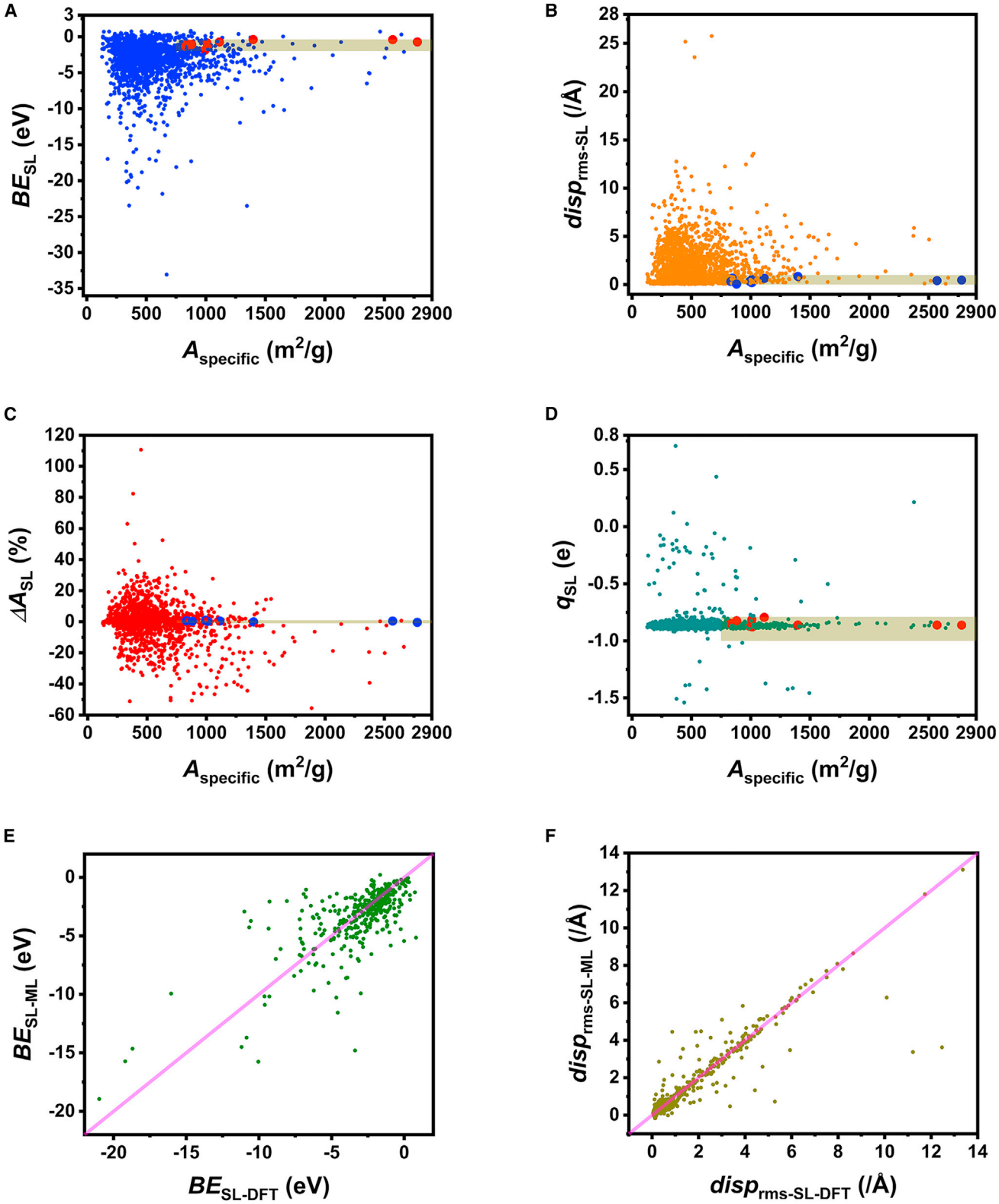

Figure 3. Data analysis and machine learning (ML) of the C2DB data for LIB applications

(A–D) The four descriptors, namely (A) BE_{SL}, (B) $disp_{rms\text{-}SL}$, (C) ΔA_{SL}, and (D) q_{SL}, are plotted with respect to $A_{specific}$. The desired range of values for high specific capacity is highlighted along with the ten shortlisted points satisfying all criteria.

(E and F) ML predicted values of (E) BE_{SL} and (F) $disp_{rms\text{-}SL}$ are plotted against their DFT predicted counterparts.

the MatErials Graph Network (MEGNet)[64] as the ideal framework to predict the FOM descriptor values. We train the network with a random 80% fraction of the dataset and varying parameters to predict the two most essential descriptors: BE_{SL} and $disp_{rms\text{-}SL}$. Figures 3C and 3D illustrate the prediction accuracy on the 20% unseen test data. For BE_{SL}, the mean absolute error (MAE) is 1.31 eV and the coefficient of determination (R^2) is 0.46, while in the case of $disp_{rms\text{-}SL,}$ these values are 0.35/Å and 0.82. Considering the range and the skewness of the data, these accuracies are indeed encouraging to tout deep learning (DL) as a rapid screening tool. Of course, the accuracy can be further enhanced by training with a larger dataset. However, the number of similar samples in the C2DB and the relatively smaller size of the dataset prompted us to investigate the predictive power of MEGNet further.

Cross-validation (CV) techniques have been a popular tool for these kinds of explorations.[67] With the same hyperparameters, we use MEGNet on the same dataset but randomly shuffled to perform a 5-fold leave-one-out CV. The MAEs obtained for the cases of BE_{SL} and $disp_{rms\text{-}SL}$ are (1.37, 1.43, 1.39, 1.31, 1.38) eV and (1.18, 1.08, 1.05, 0.89, 1.17)/Å. The average MAE for BE_{SL} (1.37 eV) from CV closely matches the performance of the previous model, indicating similar performance in randomly shuffled CV. However, the performance in the case of $disp_{rms\text{-}SL}$ (mean CV score 1.07/Å) is slightly worse than that of the previous model. Recently, a different technique named forward cross-validation (FCV) has been proposed to judge a model's performance more rigorously, especially for materials science datasets where a FOM is being predicted.[67] Here, the data are first sorted based on the property being predicted, and then, starting from a single fold of training and validation set, the training set size is increased a fold per iteration. The validation set size is kept the same, but the set number is shifted 1-fold per iteration. Again, we apply MEGNet for this test, with the same hyperparameters to the same dataset, but sorted in the ascending order of properties BE_{SL} and $disp_{rms\text{-}SL}$. The obtained MAEs are (2.57, 2.15, 1.82, 2.23) eV and (0.27, 0.65, 1.5, 3.5)/Å for BE_{SL} and $disp_{rms\text{-}SL}$, respectively. Again, considering the ascending order of the data and the smaller size of the training sets for most iterations, these values seem decent. However, the unsaturated nature of the FCV score with respect to the iteration number indicates that more data are required to train the models to increase their explorative prowess in the high-value regions.

Random structure searching for multi-Li adsorption

We use *ab initio* random structure searching (AIRSS)[26,28,47,68] to find the most stable (global minima) Li-adsorbed phase of some shortlisted materials. If the Li-adsorbed material has formula $Li_xA_yD_z$, where the pristine material is A_yD_z, we choose $0.67(y+z) \leq x \leq 2.0(y+z)$, which is a reasonable concentration range for high-specific-area materials to show high specific capacity.

Figure 4 shows the side view of AIRSS-found Li adsorbed most stable phases of 9 high-specific-area materials. The average Li binding energies (BE_{max}) for these most stable lithiated phases are tabulated in Table S1. Too large an absolute value of any descriptors results in highly deformed amorphous-like structures that clearly won't return close to the initial structure upon delithiation. The material P_2Si_6 exhibits large absolute values for BE_{SL} and ΔA_{SL} and becomes extremely deformed upon lithiation even with a relatively moderate concentration of Li. However, the material BP displays moderate values of all four descriptors and accommodates all Li-ions without any significant distortion. The structure becomes puckered from the flat freestanding form upon a full-house lithiation, but this has also been found

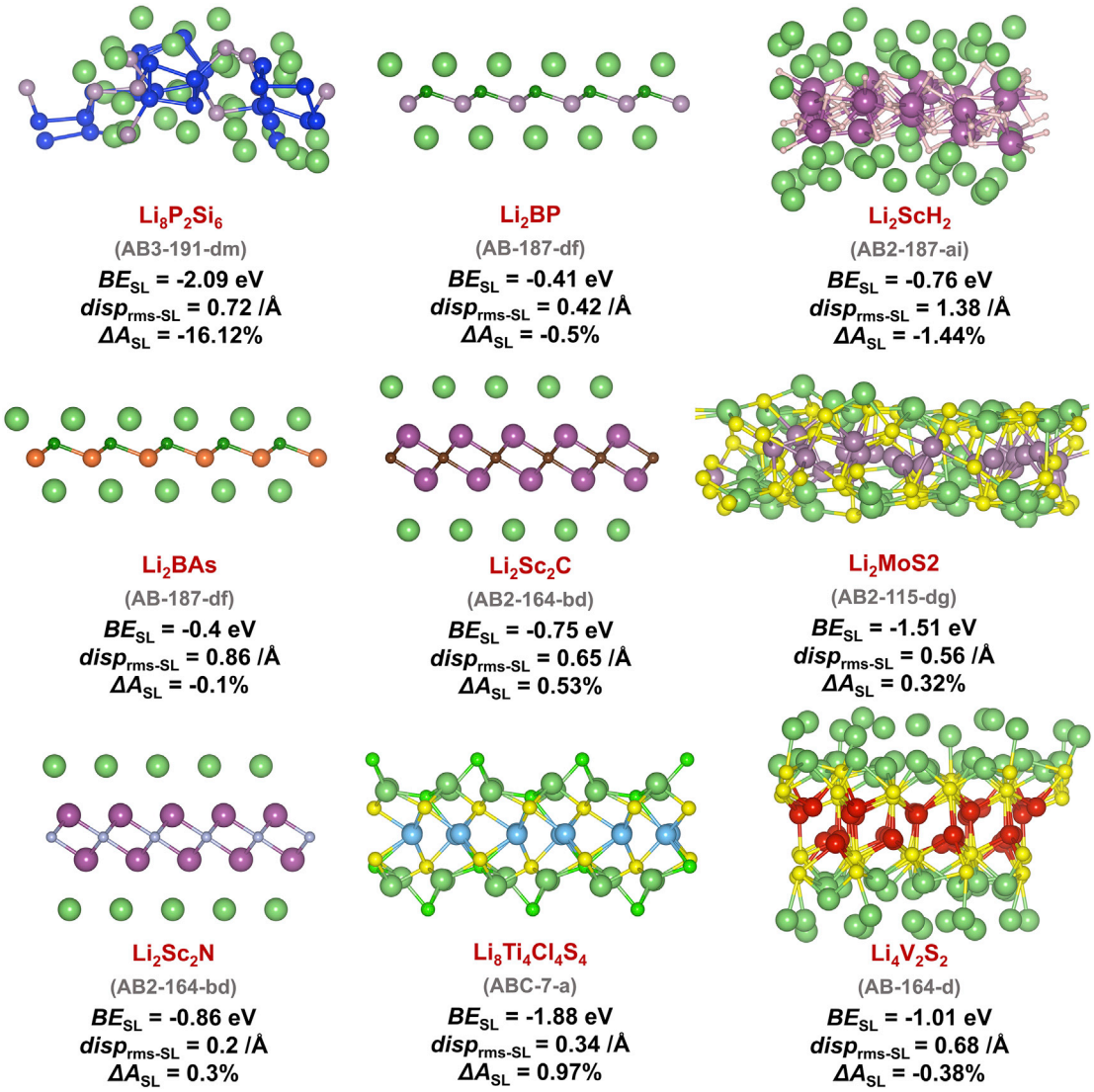

Figure 4. AIRSS-found most stable lithiated structures

The side views of the Li-adsorbed structures are shown, where the green balls above and below the materials represent the Li-ions. The light purple, dark blue, dark green, pink, dark purple, orange, brown, yellow, light blue, light green, sky blue, and red balls represent P, Si, B, H, Sc/Mo, As, C, S, N, Cl, Ti, and V atoms, respectively.

with uniform adsorption.[50] Note that our AIRSS-found most stable structure is different from this uniformly adsorbed structure where all Li ions have been placed on the hollow sites. Here, the top Li layer is adsorbed on the hollow spot, and the bottom layer is adsorbed on top of the B atom. The material BAs, where the P species is replaced with equivalent As species, also show similar behavior, both in terms of SL and full-house adsorption. The material ScH_2 delivers moderate binding energy, but the absolute values of $disp_{rms\text{-}SL}$ and ΔA_{SL} are slightly higher than 1/Å and 1%. The material becomes irreversibly damaged upon a full-house lithiation. The 2-layer bare MXenes with formula M_2X (M = Sc/Ti and X = C/N) also satisfy our initial screening criteria of $A_{specific}$ with the descriptor values falling into the desired range as well. Considering the high computational cost, we only test the lighter ones, namely Sc_2C and Sc_2N, using AIRSS. The most stable lithiated phases

accommodate a full-house of Li-ions with almost no structural distortion. Again, it should be noted that the AIRSS-found structures are different from conventional uniformly adsorbed structures.[55–59] The top Li layer here is adsorbed on top of the X atoms, whereas the ions in the bottom layer get adsorbed on top of the M atoms. These cases highlight the advantage of using AIRSS to find the most stable phase over intuition-driven manual Li placement. The material MoS_2 (AB2-115-dg) exhibits all descriptor values in the desired range. Yet, it becomes almost amorphous upon a full-house Li adsorption, possibly because the material is thermodynamically not very stable, and the most stable (at the global minima) phase of MoS_2 is the 2H phase. Nevertheless, this case shows that the SL descriptors could fail to predict what happens at full-capacity Li adsorption for a few materials. The material $Ti_4S_4Cl_4$ is an alloy originating from the H-phased TiS_2, where 50% S atoms of both sides have been replaced with Cl atoms. This material also falls in our desired range in terms of descriptors. Interestingly, the AIRSS-found structure does look somewhat close to a uniformly adsorbed structure, but it seems the material turns into an H′ phase with metal atoms forming periodic clusters. The Cl atoms at the intra-cluster space seem to be popping out of the plane, but the base of the structure appears primarily unharmed. We perform a "quick delithiation"[28] test on this structure and find that the material returns precisely to its starting phase after the delithiation (Figure S2), indicating the changes with lithiation are entirely reversible. The material V_2S_2 undergoes severe structural deformations upon lithiation, and layered adsorption of Li-ions in the most stable structure can be observed. However, after quick delithiation, the structure seems to be returning close to its original form (Figure S2). These two materials can be categorized as "borderline cases," where despite showing severe structural changes with a high concentration of Li adsorption, the materials return to their pristine form upon delithiation. This highlights the predictive power of the defined SL descriptors, which can indeed work for non-trivial borderline cases.

Electrolyte test and passivation strategy for Li-ion storage

After the random-structure-searching-based reversibility test, we examine the top-performing materials' reactivity with commercially available LIB electrolytes, ethylene carbonate (EC) and dimethyl carbonate (DMC). Silicene visually does not show any signs of reacting with the EC molecule (Figure S3), and the binding energy (−0.36 eV) is almost fully contributed (88.53%) by dispersion energy. The materials BP and BAs also do not visually seem to be reacting with the electrolyte, but these do show a mild deformation upon EC adsorption (Figure S3). Again, the binding energy (−0.36 eV for BP and −0.37 eV for BAs) is entirely contributed (96.67% for BP and 98.54% for BAs) by dispersion energy, indicating these materials are inert to EC and are ideal to be wetted by the electrolyte. The material $Ti_4Cl_4S_4$ visually does not show any deformation after the adsorption of EC, but V_2S_2 does (Figure S3). However, in both the cases again, the binding energy (−0.44 eV for $Ti_4Cl_4S_4$ and −0.55 eV for V_2S_2) is mainly contributed (87.96% for $Ti_4Cl_4S_4$ and 68.88% for V_2S_2) by the dispersion energy; thus, almost no chemical reactivity and good wetting is expected.

Despite surviving the AIRSS test with flying colors, the MXene group, M_2X, intuitively seems reactive and prone to oxidation as these have bare metal surface terminations. In fact, functionalization with various functional groups is an extremely popular strategy for MXenes to reduce the reactivity of the surface as well as tune the properties.[69,70] As expected, all four shortlisted M_2X materials react violently with both the EC and DMC, which visually results in the disintegration of the molecules (Figure 5; Figure S4). Also, the contribution of dispersion energy to the highly negative binding

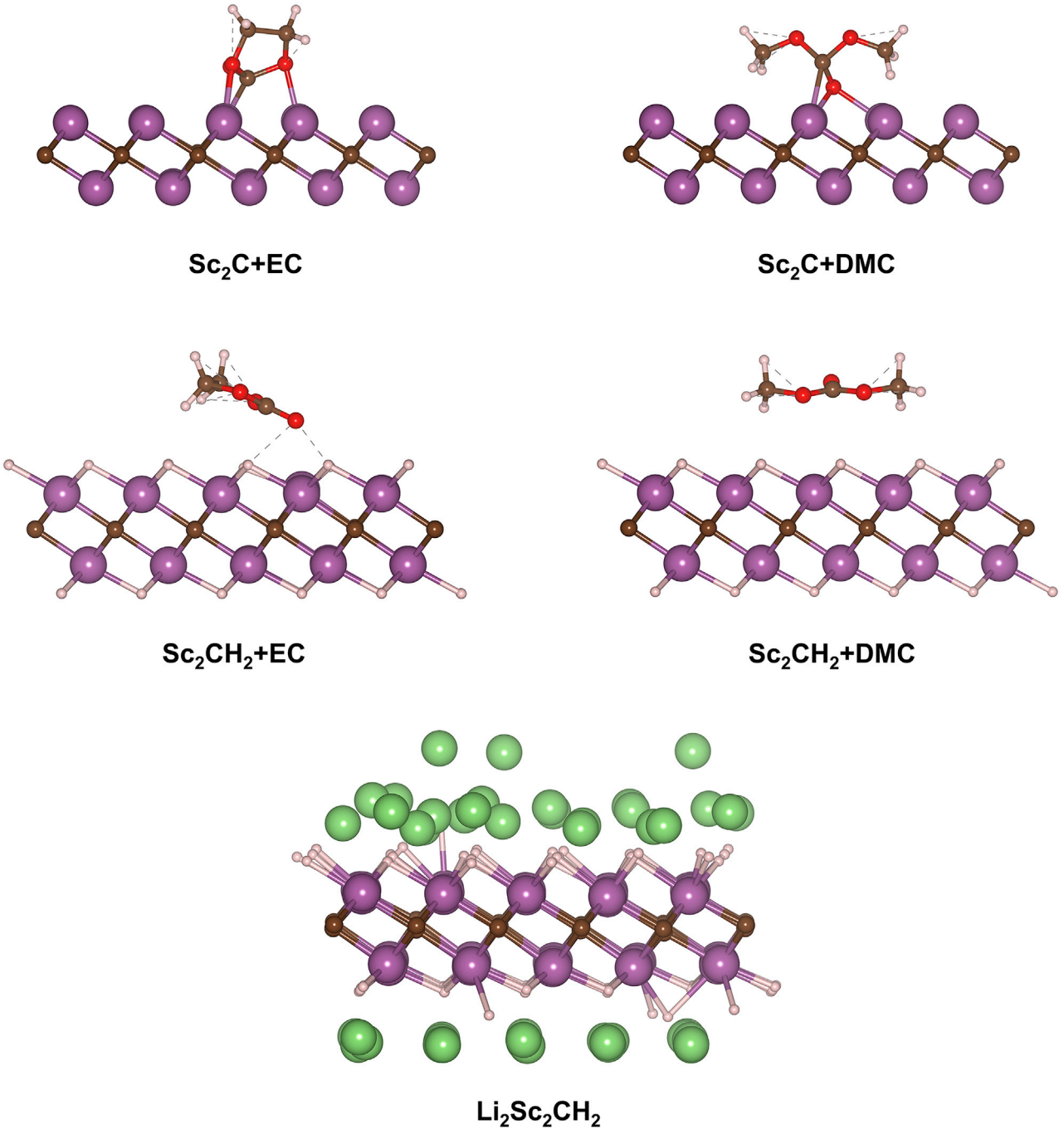

Figure 5. Electrolyte reactivity, hydrogen passivation, and Li storage of Sc_2C

The color convention of Figure 4 has been repeated, except the red balls represent the oxygen atoms here. The dotted lines signify hydrogen bonds.

energy is minimal (Table S2). Clearly, functionalization is required to suppress the reactivity of the metal surfaces. Surface passivation by hydrogen is a popular and relatively easy technique that has recently been successfully used to passivate and stabilize borophene in ambient conditions.[71] Moreover, among all functional groups, H-functionalization adds minimum molar weight to the material, which in turn helps to preserve the specific capacity. Taking the lightest material, Sc_2C, as an example, we

Table 1. Specific capacity and specific capacitance of some noteworthy materials

Material	Specific capacity (mAh/g)	Specific capacitance (F/g)
C2_A-191-d (graphene)	0	122.38
MoS2_AB2-187-bi (2H-MoS_2)	272.08	42.54
Si2_A-164-d (silicene)	954.11	296.28
Honeycomb borophene*	2,479.28	537.39
Beta-aluminene*	993.36	220.87
BP_AB-187-df	1,282.96	152.66
AsB_AB-187-df	625.24	88.38
Sc2C_AB2-164-bd*	525.92	144.29
Sc_2CH_2	515.70	104.91
Sc2N_AB2-164-bd*	515.8	143.67
Sc_2NH_2	506.01	119.69
Ti4Cl4S4_ABC-7-a	464.54	91.54
V2S2_AB-164-d	645.77	91.06
Ti_2BH_2	493.75	111.57

The materials marked with asterisk exhibit highly reactive surfaces.

functionalize it with hydrogen and test the adsorption behavior for both EC and DMC. The binding energy, contributed mainly by dispersion, becomes significantly less negative (Table S2). Visually, the structures also seem almost unperturbed (Figure 5; Figure S4), except for the formation of weak hydrogen bonds between the oxygen of the EC molecule and hydrogen of the surface. In absence of chemical reactivity, this would aid in better wetting. Next, we test Sc_2CH_2 through AIRSS again, with the same amount of Li content as before. The most stable structure shows moderate distortion in the surface consisting of hydrogen, but the base of the material remains intact. It is worth noting that this structure is only negligibly (0.004 eV/atom) more stable than the uniformly adsorbed structure. The original material is fully recovered after quick delithiation (Figure S2). The specific capacity decreases negligibly compared with its bare counterpart as mentioned in Table 1. Therefore, for reactive materials, hydrogen passivation seems to be the best way to suppress the reactivity while keeping the specific capacity almost intact.

ML-driven discovery of LIB electrode materials

Based on the ML-based screenings, we prepare another small set of data with 22 materials (Data S2), where eight materials are shortlisted from the Jarvis-2D database.[31,32] In addition, we also include all the synthesized phases of borophene,[47] M_2Y MBenes (M = Sc/Ti/V and Y = B),[55] hydrogen-functionalized M_2XH_2 and M_2YH_2 (M = Sc/Ti/V, X = C/N Y = B), 2H-MoS_2, and highly asymmetric 1T′-ReS_2.[28] After performing our high-throughput SL calculations, only eight materials, namely β_{12}, striped and χ_3 borophene, Ti_2B, Ti_2CH_2, Sc_2CH_2, Ti_2BH_2, and Sc_2NH_2, exhibit SL descriptor values in the desired range. Sc_2B and Sc_2BH_2 show high ΔA_{SL}. Indeed, the AIRSS-found most stable lithiated structure of Sc_2BH_2 (Figure S5) is an almost amorphous structure where the B atoms form clusters by coming together, indicating weak Sc–B bonds. Remarkably, both Ti_2B and Ti_2BH_2 exhibit all descriptor values in the "sweet spot." The AIRSS-found most stable structure is also the uniformly adsorbed structure (Figure S5), indicating Ti_2BH_2 could be an excellent material for LIB anode application. It is worth mentioning that both the SL binding energy and charge transfer is somewhat poor in Ti_2BH_2, but these quantities improve drastically through a subtle structural change with a "full-house" of Li adsorbed. The β_{12}, striped, and χ_3 borophenes have already been established as excellent LIB anode materials by global-minima-search-based previous study.[47] These results reaffirm our choice of range for the descriptor values. The only exception in this set is the

honeycomb borophene, which shows extremely out-of-range values for the first 3 descriptors, yet is touted to have extremely high specific capacity.[72] However, it should be noted that the pristine honeycomb phase is the most unstable borophene by quite a distance[47], and it exists in an electron-deficient form naturally and stabilizes only on Al[111] by adsorbing electrons from the surface.[10,73] Closer inspection reveals that the honeycomb borophene transitions into a mixture of β_{12} and χ_3 phase upon SL adsorption, characterized by the material's extremely negative BE_{SL} and extremely high single-Li adsorption-induced structural changes. As expected, adsorption of EC molecule also induces phase change in the material, revealing charge transfer and chemical reactivity (Figure S6; Table S2).

Modeling of electrode-electrolyte systems for supercapacitors

We begin the supercapacitor part of this work with a brief overview of the essential physical and computational parameters chosen for the selected computational framework. Only materials with a PBE bandgap of less than 2 eV have been selected since the wider bandgap materials would have extremely low electronic conductivity and thus would be unsuitable for electrode applications. For instance, monolayer MoS_2 shows an experimental bandgap close to 2 eV,[74] and MoS_2 nanowalls-based supercapacitors have been reported to show a specific capacitance ($C_{specific}$) of around 100 F/g,[75] slightly less than that of graphene.[24,25] We use the solvation model SaLSA (Spherically Averaged Liquid Susceptibility Ansatz) for all calculations that simulate a 6 M aqueous electrolyte. SaLSA is a fully non-empirical solvation model that captures the atomic-scale nonlocality of the fluid response at a linear-response level.[15] All the essential parameters and models have been chosen after rigorous benchmarking tests. More computational details and the results of the benchmarking tests are described in the Experimental procedures and Supplemental information sections.

A total of 3,691 materials from C2DB possessing a bandgap less than 2 eV have undergone our fully automated computational framework (Data S3) detailed in Figure 1. The lattices and ionic positions of the materials are first optimized in a vacuum and then a neutral or zero potential calculation with the material immersed in the implicit non-adsorbing electrolyte is performed to find out the potential of zero charge (PZC). After that, fixed-potential grand canonical JDFT calculations are performed where the potential of the material is varied in the range $V \in [-0.6\ V, 0.6\ V]$ around the PZC. With the fixed potential simulating the applied voltage in a capacitor plate, the surface charge density on the electrode (Q) is calculated from self-consistent JDFT that simulates the electric double-layer (EDL) formation at the interface of the solid and the electrolyte. Usually, the integral capacitance is defined as $C_I = Q/(V\text{-PZC})$. However, due to some observed discontinuities of the V-Q curve for a few materials, in this work, we take the quantity average integral capacitance (C) as the fundamental capacitance of a material, which is obtained by calculating the slope of the best linear fit to the V-Q curve. Such a fitting technique also equips us with the squared sum of the errors, termed as the residual error ($E_{residual}$), as a measure to estimate the amount of nonlinearity or discontinuity in the curve. Such nonlinearity or discontinuity of the V-Q characteristic is an undesired consequence of charge asymmetry correction in the semi-empirical charge-asymmetric nonlocally determined local-electric (CANDLE) model and might yield unphysical results.[20,21] In fact, we first attempted to use CANDLE for our work, and after assessing almost 70% of the materials, we did observe a large discontinuity in the V-Q curve for a significant number of materials. The non-empirical but computationally expensive SaLSA model reduces this number significantly. Graphical processing units (GPUs) are used to manage this additional computation load for our high-throughput study.

It is worth mentioning that when the capacitive response is nearly linear, SaLSA and CANDLE yield almost identical results (Figure S7; Table S3). However, when the curve shows nonlinear nature with CANDLE, the value C becomes highly overestimated compared with SaLSA (Figure S8; Table S4).

Data analysis of electrode-electrolyte systems

All calculations of 3,691 materials from C2DB have finished gracefully with our automated high-throughput computational framework, and their capacitive properties are determined. Figure S9 and Table S5 show a statistical description of four important quantities from these data: specific area, PZC, specific capacitance, and residual error. The PZC is a vital quantity that determines the electrochemical voltage window of charging for a particular electrode-electrolyte interface. However, as discussed in the Supplemental information (Figures S10 and S11) and Experimental procedures, the PZC calculation of our high-throughput methodology may not be very reliable for strongly correlated materials. The other quantities, however, can be calculated with high reliability. Both the mean and median values of the PZC turned out to be −0.14 V versus the standard hydrogen electrode (SHE), somewhat close to that of graphene (−0.68 V versus SHE). Also, the PZC data are skewed toward the negative tail. This implies most materials of the database can operate in the voltage windows of commonly used electrolytes such as aqueous KOH as these have been successfully used with graphene electrodes.[23–25] We also demonstrate in the Supplemental information that the specific capacitance of a material is almost independent of the solvent or the electrolyte used. Non-aqueous organic electrolytes can provide a much larger voltage window of operation. Therefore, the PZC value determined in this work might not be an ideal parameter for screening suitable electrode materials for supercapacitors. However, the specific capacitance is much more universal and might be the perfect parameter to judge a material's supercapacitive performance. The mean and median value of $C_{specific}$ is 71.97 and 51.54 F/g, respectively, and the data are skewed toward the positive axis (Figure S9; Table S5). The poor mean and median values indicate that most 2D materials in the database exhibit low $C_{specific}$.

As expected, we observe a strong linear relation between specific area ($A_{specific}$) and $C_{specific}$ (Figure 6A). A large $A_{specific}$ often results in a decent $C_{specific}$, although there are exceptions where the average integral capacitance plays the dominating role. The $E_{residual}$ versus $C_{specific}$ plot (Figure 6B) reveals that most of these materials exhibit linear capacitive responses. However, 4.63% of materials show $E_{residual}$ > 10 $\mu C^2/cm^4$, while 3.71% show $E_{residual}$ > 100 $\mu C^2/cm^4$, elucidating highly nonlinear or even a discontinuous V-Q relationship. Such nonlinearity has been observed experimentally with Ag[100] surface near the PZC,[76], but there is a lack of continuum solvent model to represent this behavior accurately.[21] The material FeH_2O_2_AB2C2-12-ci exhibits $C_{specific}$ = 1,014.24 F/g and $E_{residual}$ = 1,331.45 $\mu C^2/cm^4$, and according to C2DB shows high dynamic and medium thermodynamic stability. For this material, using various available solvation models, we show that none of them can rectify the discontinuous nature of the response, but SaLSA and LinearPCM-GLSSA13 produce the least $E_{residual}$ (Figure S12; Table S6). However, for a similar material, H_2O_2Sb_AB2C2-12-ci, SaLSA produces near-zero $E_{residual}$, whereas CANDLE produces $E_{residual}$ = 5,517 $\mu C^2/cm^4$ (Figure S8; Table S4). These examples show that SaLSA can consistently outperform the other models, possibly because of its non-empirical nature. However, we are unable to comment on the origin or the physical feasibility of such discontinuity of the V-Q curve, and further probing and refinement of models are required.[21] Figure 6C shows how the PZC is distributed with respect to the $C_{specific}$. A small cluster can be observed on the bottom right

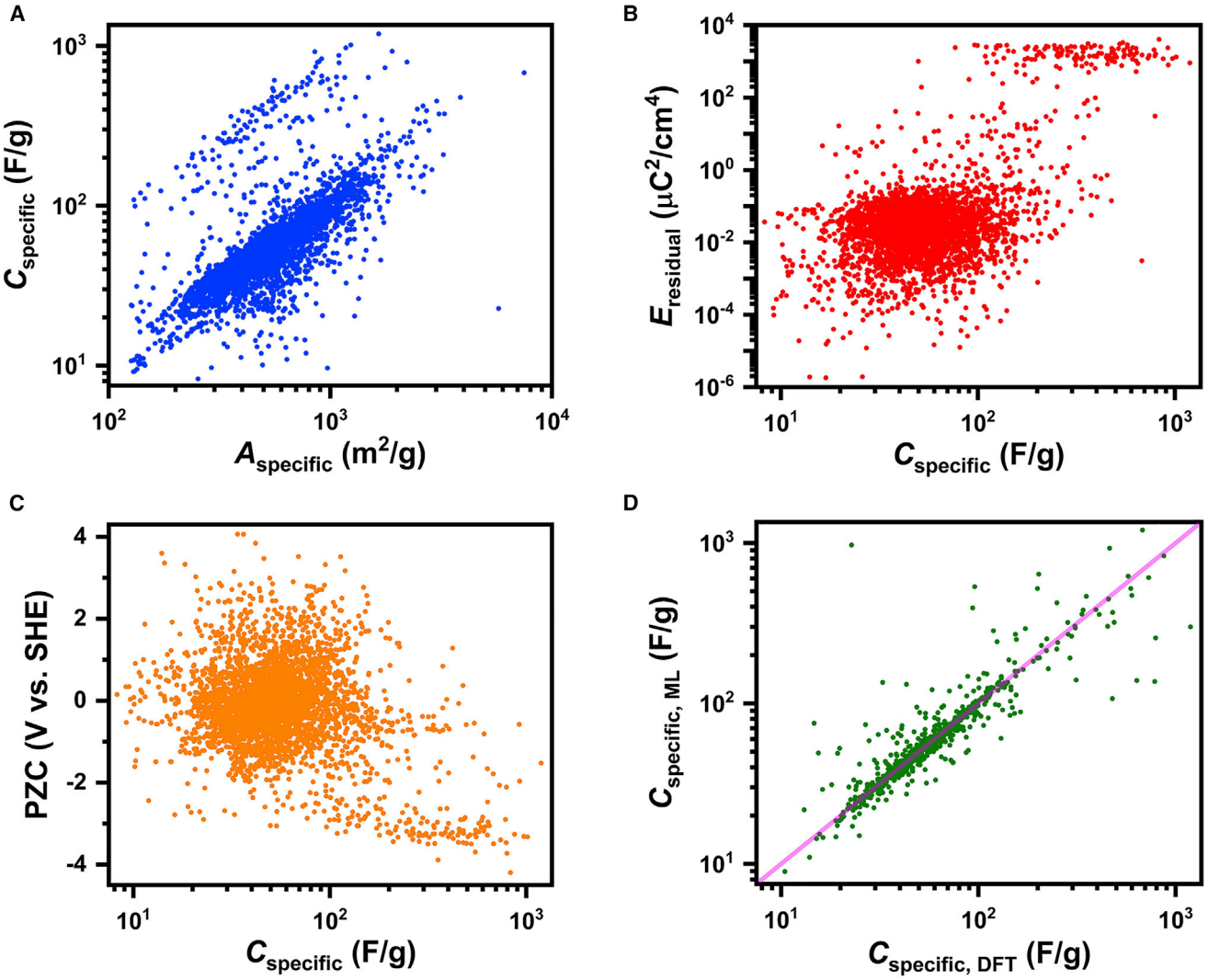

Figure 6. Graphical representation of various important quantities obtained from probing the capacitive responses of materials from C2DB

(A–D) Plots of (A) specific area versus specific capacitance, (B) specific capacitance versus residual error, (C) specific capacitance versus PZC, and (D) (J) DFT-predicted specific capacitance versus ML-predicted specific capacitance for a test set not seen by the model.

of Figure 6C, indicating high $C_{specific}$ and highly negative PZC. These are mostly the strongly correlated materials, where the PZC calculation can be erroneous.

ML and discovery of supercapacitor electrode materials

We further use MEGNet to develop a model to predict the average integral capacitance, the intrinsic chemical property of a material. It can then be scaled by $A_{specific}$, directly obtainable from the crystal structure, to acquire a prediction of $C_{specific}$. The C2DB data are partitioned into a random 0.8:0.2 train-test split to train and test the models with varying parameters. The best model displays an impressive MAE of 2.07 μF/cm^2 and an R^2 of 0.7, with 739 (20%) unseen test data points. It translates to an MAE of 18.1 F/g in terms of $C_{specific}$. The model's performance on the test data is shown in Figure 6D. As defined in the section for SL-ion properties, here we also perform 5-fold CV and FCV tests on the dataset, randomly shuffled for the former and sorted in ascending order of C for the latter, to rigorously examine the explorative power of MEGNet. The obtained MAEs are (1.95, 2.15, 2.34, 2.08,

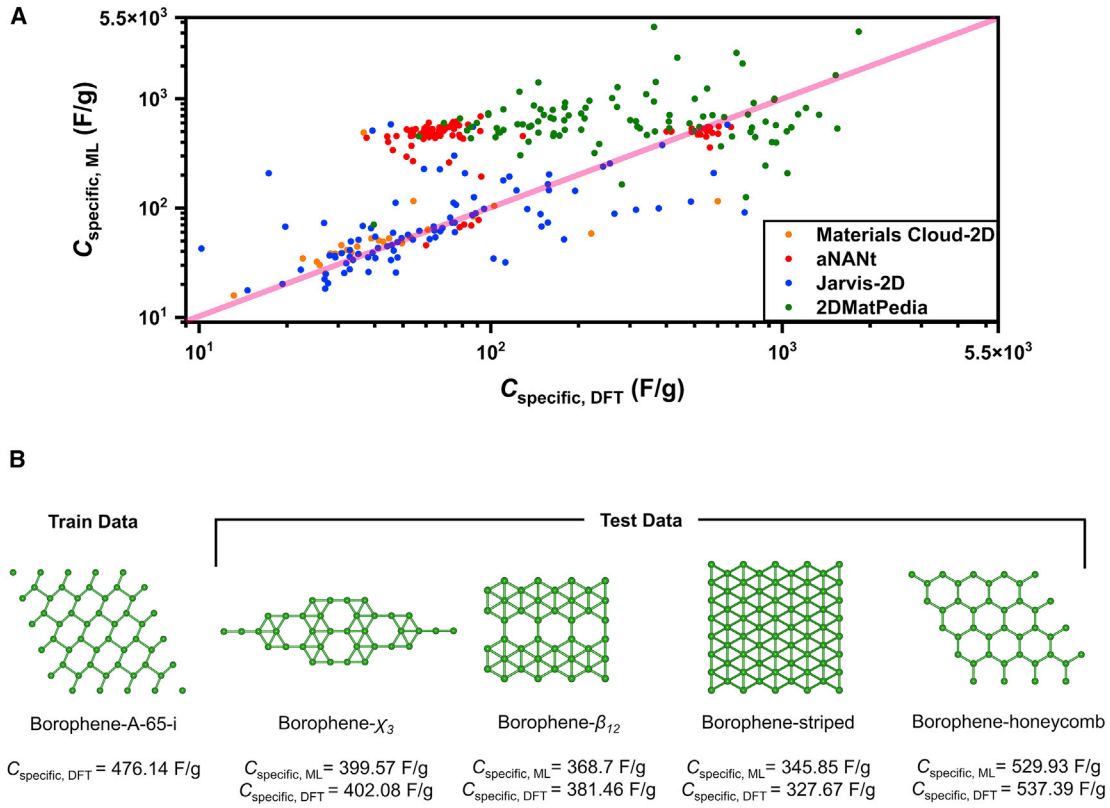

Figure 7. Performance of the ML model and discovery of new materials from other databases using ML

(A) The plot of (J)DFT-predicted specific capacitance versus ML-predicted specific capacitance for 327 materials shortlisted from 4 different databases.

(B) The ML model's prowess demonstrated on borophene polymorphs.

2.17) μF/cm^2 for 5-fold CV (mean CV test score = 2.14 μF/cm^2) and (1.77, 1.34, 1.51, 14.24) μF/cm^2 for 5-fold FCV. Again, these scores seem decent and on-par in terms of performance with the previous model. The extremely high value of MAE (14.24 μF/cm^2) for the last fold of FCV could be due to two reasons. First, the large range and ascending order of data are partially responsible. Second, as described before, the high values of C and $C_{specific}$ mostly come from highly nonlinear or even a discontinuous V-Q relationship, the physical feasibility of which is doubtable and could simply originate from the limitations of the SaLSA model.

Using this model as a quick screening tool, we thoroughly search four other 2D-materials databases, namely, Materials Cloud-2D,[29] aNANt,[30] Jarvis-2D,[31,32] and 2DMatPedia,[33] to discover materials with high $C_{specific}$. To diversify the data for future training, about 20% of materials were shortlisted with low-to-moderate $C_{specific}$, whereas the rest are predicted to have a large (>500 F/g) $C_{specific}$. After another set of JDFT calculations on this new dataset, we end up with a total of 327 new materials, excluding the overlapping data and failed calculations. The model produces MAE = 29.93 μF/cm^2 and R^2 = −1.72 for this dataset. The performance in terms of $C_{specific}$ is illustrated in Figure 7A, and the MAE in terms of the same is 266.93 F/g. The model performs well on Materials Cloud-2D, Jarvis-2D, and part of the aNANt dataset. However, it performs poorly on the data from 2DMatPedia and a large part of aNANt. We have observed this kind of behavior in a previous work,[37] as most structures of 2DMatPedia can be drastically different from other databases. When the data from 2DMatPedia and aNANt are excluded

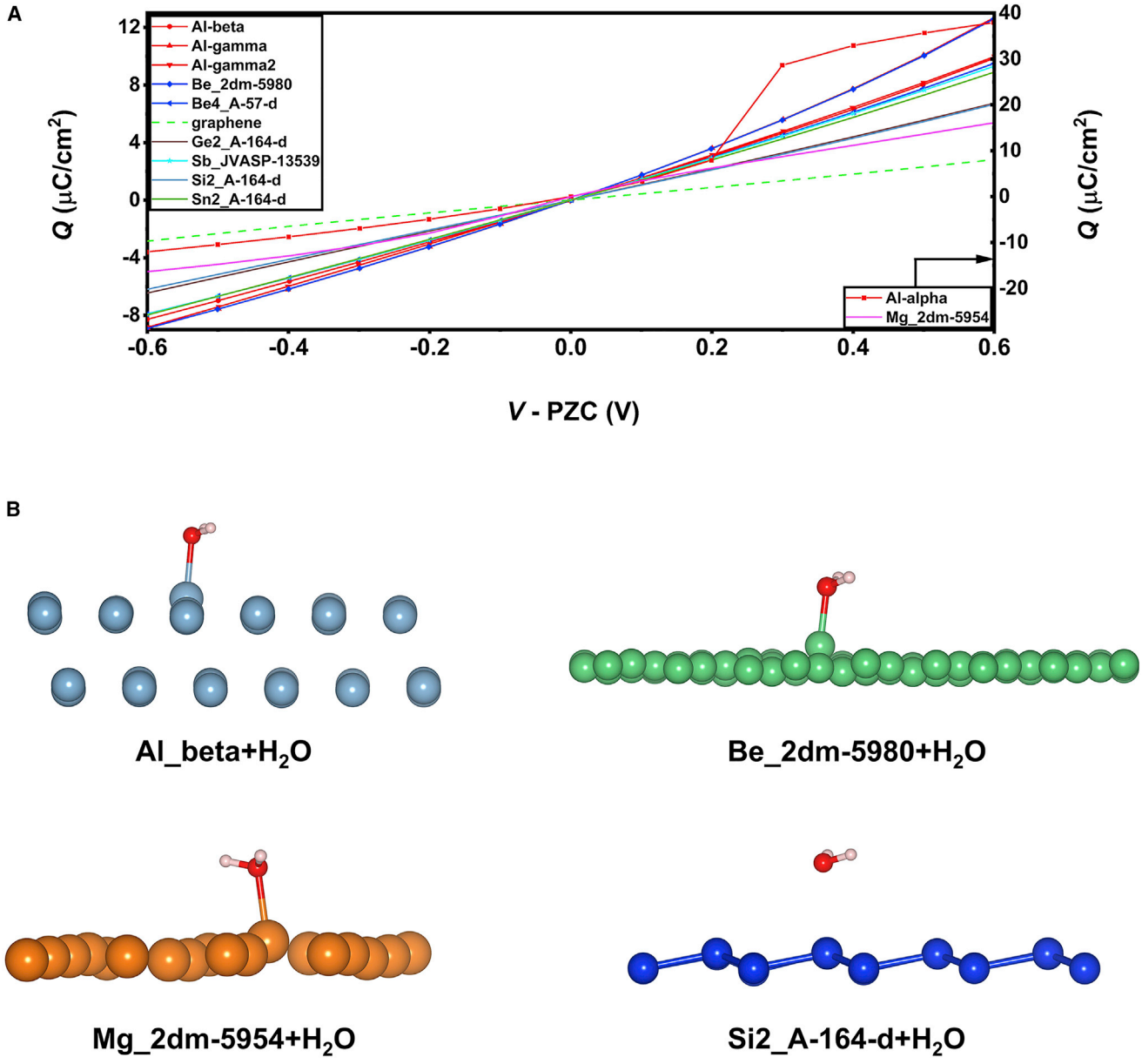

Figure 8. Monoelemental 2D materials as supercapacitor electrodes

(A) Capacitive performances of promising and unexplored monoelemental 2D materials. The *V*-*Q* curves of Al-alpha and Mg_2 dm-5954 have been referenced with the right-sided y axis to cover their larger range.

(B) Structure of monoelemental 2D materials with an adsorbed water molecule. The gray, green, orange, and blue balls represent Al, Be, Mg, and Si atoms, respectively.

from the test dataset, the MAE improves considerably to 8.5 μF/cm^2 and 29.78 F/g in terms of C and $C_{specific}$, respectively. The improved R^2 score, however, still remains negative with a value of −0.8. Although the model's overall performance seems to be poor here, it performs exceptionally well in some important cases. One such case is highlighted in Figure 7B. The present version of C2DB contains only a single phase of borophene, the unstable A-65-i polymorph, which was part of the training data. Upon testing the model on experimentally synthesized borophene phases,[73,77,78] we got an MAE of 10.23 F/g and excellent individual accuracy in

terms of $C_{specific}$, which is illustrated in Figure 7B. It can be observed that the A-65-i borophene is structurally very dissimilar from the experimental synthesized phases. Also, there is a moderate amount of structural variation among the synthesized allotropes. Yet, the ML model's learning capability to produce such accurate predictions is indeed remarkable.

Supercapacitance of monoelemental 2D materials

Monoelemental 2D materials, such as borophene, silicene, and aluminene, have recently been predicted to show ultra-high Li-ion storage capacity for LIB applications.[47] The light molar weight and high charge conductivity of these materials also make them suitable candidates for supercapacitive applications. Figure 8A shows the capacitive performances of a host of unexplored light monoelemental 2D materials exhibiting a better integral and specific capacitance than graphene. These are as follows: 2D magnesium (Mg_2 dm-5954, 1828.51 F/g), all four predicted phases of aluminene (220.87–1,712.6 F/g), two 2D allotropes of beryllium (Be_2 dm-5980 and Be_4_A-57-d, 940.2 and 393.46 F/g), silicene (Si_2_A-164-d, 296.29 F/g), stanene (Sn_2_A-164-d, 134.15 F/g), germanene (Ge_2_A-164-d, 128.83 F/g), and antimonene (Sb_JVASP-13539, 122.57 F/g). All of these are predicted to have either metallic nature or a very low bandgap (0.02–0.06 eV), elucidating ideal conductivity for supercapacitor electrodes. However, it should be noted that Mg_2 dm-5954 shows slightly discontinuous *V*-*Q* characteristics in our calculations.

The metal atom terminations for most monoelemental materials hint that they could be highly reactive even in aqueous electrolytes and prone to oxidation. To test the reactivity of the top-performing four monoelemental 2D materials, we place a water molecule in proximity to them and perform atomic relaxations. The relaxed structures are shown in Figure 8B. Expectedly, the first three materials, namely beta-aluminene, monolayer beryllium, and monolayer magnesium, react vigorously with oxygen from the water molecule, showing definitive structural changes in the material and chemical bond formation between the metal ions and oxygen with very low dispersion energy contributing to the strong binding (Table S2). This indicates that our implicit electrolyte model may not be valid for these materials. Silicene however does not chemically react with water at all, but interacts through weak van der Walls force, implying the used implicit electrolyte model is valid in this case, and silicene indeed is a potential material with excellent supercapacitive performance.

DISCUSSION

Combining the "explicit-ion" and "implicit-solvent" formalisms, we discover certain materials (Table 1) that show desirable specific capacity for LIB applications and specific capacitance for supercapacitive applications. The specific capacity of the materials has been determined from the AIRSS results, like previous works,[28,47] and the electrolyte test with EC and DMC has been performed later. On the other hand, the supercapacitive properties are determined from an implicit electrolyte model with parameters tuned for aqueous solvent. We show in Figure S13 and Table S7 that, usually, the exact type of solvent affects the specific capacitance minimally; therefore, the determined specific capacitance values should be transferable to other electrolytes as well.

The first two entries of Table 1, graphene and 2H-MoS_2, are arguably the two most studied 2D materials, and their FOMs are given for comparative analysis. The materials marked with an asterisk, namely honeycomb borophene, beta-aluminene, Sc_2C, and Sc_2N, are proven to be highly reactive to common solvents. Other phases of

borophene are not reactive toward common electrolytes (Figure S6; Table S2).[79] Silicene has been demonstrated as an excellent material for both LIB (954.11 mAh/g) and supercapacitive (296.28 F/g) applications, owing to its high specific area and inert-to-electrolyte surfaces. BP shows excellent specific capacity (1,282.96 mAh/g) and decent specific capacitance (152.66 F/g), whereas BAs, $Ti_4Cl_4S_4$, and V_2S_2 show good specific capacity (625.24, 464.54, and 645.77 mAh/g, respectively) but moderate specific capacitance (88.38, 91.54, and 91.06 F/g, respectively). Hydrogen-passivated MXenes Sc_2CH_2 and Sc_2NH_2, and MBene Ti_2BH_2 show good Li-storage (515.70, 506.01, and 493.75 mAh/g) and specific capacitance (104.91, 119.69, and 111.57 F/g) close to that of graphene (122.38 F/g). It is worth mentioning that experimentally, the specific capacitance of graphene and MoS_2 has been found to be up to 135[24] and 100 F/g,[75] which indicates that our calculated $C_{specific}$ values may be underpredicted, and the real specific capacitance of the materials mentioned above can be even higher.

Although the ML models perform encouragingly when the data are randomly split, results from more extensive tests such as FCV suggest that the models are not performing satisfactorily in terms of extrapolative prowess, and more data are required to train the models to the desired accuracy. However, the ML component is not the primary focus of this study. The ML tool's main goal was to quickly scan through various databases, searching for "promising" electrode materials for LIB and supercapacitor applications, which has mostly been fulfilled.

In summary, we have predicted the performances of a few thousand 2D materials as LIB and supercapacitor electrodes using fully automated explicit-ion-DFT-based and implicit-electrolyte-JDFT-based calculations. For Li-ion storage, four descriptors were defined based on the SL-binding properties, which are much easier to obtain compared with the gold standard of global minima searching. A clear range of values for these descriptors were empirically determined that helps in finding potential materials with high specific capacity. An ML-based model is also trained on these data that can bypass the SL DFT calculations and aid in rapid screening. For supercapacitor applications, the specific capacitance was directly determined as the implicit electrolyte model reduces the computational cost. An ML model was also developed for faster determination of capacitance. Various 2D materials with high specific capacity and capacitance have been identified, which may guide the experimentalists to engineer exceptional LIB/supercapacitor/hybrid devices capable of meeting society's ever-growing demand for energy storage.

EXPERIMENTAL PROCEDURES

Resource availability

Lead contact

Further information and requests for resources and materials should be directed to and will be fulfilled by the lead contact, Santanu Mahapatra (santanu@iisc.ac.in).

Materials availability

The crystal structures of unique materials generated in this study are available from the lead contact without restriction.

Data and code availability

The authors declare that the main data supporting the findings of this study are available within the paper and its supplemental files. The Li-ion and supercapacitor datasets are available with this paper in comma-separated values (CSV) format. The same datasets in pickled dataframe format, along with the exported and zipped ML

models, are available at https://doi.org/10.6084/m9.figshare.14406740. Other relevant data are available from the lead contact upon reasonable request.

DFT calculation setup for explicit-ion system

DFT calculations are carried out using the generalized gradient approximation (GGA) as implemented in the code Vienna Ab initio Simulation Package (VASP)[80–83] with the Projector-Augmented-Wave (PAW)[84] method using the PBE[85] exchange-correlation functional. The Materials Project recommended pseudopotentials (https://docs.materialsproject.org/methodology/pseudopotentials/) have been used throughout, except for Li, where the standard variant (without any suffixes) has been used because of its lower cutoff energy requirement. Sufficiently large cutoff energy of 520 eV is used to avoid any Pulay stress. For all structural relaxations, a $> \frac{30}{a} \times \frac{30}{b} \times 1$ Gamma-centered *k*-points grid is used to sample the Brillouin zone (BZ), where *a* and *b* are the lattice parameters of the particular supercell in Å. A $> \frac{60}{a} \times \frac{60}{b} \times 1$ similar *k*-mesh is used for all static runs. Electronic convergence is set to be attained when the difference in energy of successive electronic steps becomes less than 10^{-6} eV, whereas the structural geometry is optimized until the maximum Hellmann-Feynman force on every atom falls below 0.01 eV/Å. A large vacuum space of $\geq$25 Å in the direction of c is applied to avoid any spurious interaction between periodically repeated layers. Semiempirical dispersion corrections with DFT-D3 method as developed by Grimme et al.[86] have been used in all the calculations. All crystal structure visualizations have been done using the tool VESTA.[87]

AIRSS setup for multi-Li-ion adsorption

For the top-down random-structure searches, Li-ions are placed on top and bottom of the adsorbent supercell randomly using the AIRSS initial configuration generation engine. They are subsequently relaxed to their nearest local minima using DFT. The AIRSS code developed by Pickard and Needs[68] has been used for this purpose. The (*x*, *y*) fractional coordinates of the Li-ions are allowed to be completely random. The minimum separation between the atom pairs is kept between 1.2 and 1.6 Å to minimize atomic overlaps depending on the atomic radii. The vertical distance (along **c**) of the adsorbates from the surface is chosen randomly from the range of 2.2–3.8 Å, the usual range for typical Li-ion adsorption. More than 150 random structures that could be relaxed successfully are explored for each search. The AIRSS lowest energy phase-finding algorithm and its highly parallel master-slave implementation are similar to our previous works.[28,47] Both *a* and *b* lattice parameters of the substrate supercells are kept more than 15 Å long, and a gamma-point-only *k*-mesh is used to relax the structures while searching for the lowest energy phases. However, the top five lowest-energy structures from every energy-rank list are processed further with the above-mentioned stringent DFT setup.

JDFT calculation setup for electrode-electrolyte system

All (J)DFT calculations involving implicit electrolytes have been performed using JDFTx.[22] For the high-throughput computations for assessing the supercapacitive properties, the following DFT settings are used.

For the lattice optimizations, both the ionic positions and in-plane lattice parameters have been allowed to change. A total of 3 consecutive lattice optimizations are performed to ensure proper convergence, and the force on every atom has been confirmed to go below 0.00019 Hartree/Bohr (0.01 eV/Å). For all calculations (lattice optimization, neutral, and fixed-potential), the Perdew-Burke-Ernzerhof GGA (gga-PBE)[85] exchange-correlation has been used along with an electronic plane-wave cutoff energy of 30 Hartree, a charge density cutoff of 150 Hartree, and a Fermi function-based smearing

at T = 0.01 Hartree. A Pulay algorithm (electronic-*scf*.) with an energy convergence criterion of 10^{-8} Hartree (for more than two self-consistent field iterations) is used to find the electronic ground state. For the lattice optimizations and single-point calculations, a $\frac{60}{a}\times\frac{60}{b}\times$ 1 and a $\frac{100}{a}\times\frac{100}{b}\times$ 1 *k*-points grid is used to sample the first BZ, respectively, where *a* and *b* are the in-plane lattice parameters in Bohr. The Schlipf-Gygi 2015 (SG15)[88] norm-conserving pseudopotentials have been used for most calculations. However, for some materials, especially materials containing Re, Hg, and Be, the SG15 pseudopotentials fail. In these cases, the Garrity-Bennett-Rabe-Vanderbilt (GBRV)[89] ultrasoft pseudopotential has been used. Our benchmarking tests show that both of these pseudopotentials produce nearly identical results (Figure S14; Table S8), but the SG15 is preferred as it is slightly faster.

While choosing the proper solvation model among many available choices,[15–17,90–92] it is imperative to balance accuracy and speed for a high-throughput study like ours. The LinearPCM-CANDLE continuum solvation model is the latest and recommended for most applications by the authors of JDFTx.[16] On the other hand, the SaLSA solvation model directly captures the nonlocal response of the liquid using an angular momentum expansion and determines the cavity from an overlap of solute and solvent electron densities.[15] According to the authors, this model is usually a factor of 10 more expensive than the continuum solvation models such as CANDLE or GLSSA13. Basically, with a much faster speed, CANDLE mimics the response of SaLSA empirically. For more details, please see the JDFTx website (https://jdftx.org). CANDLE has also been successfully used in a similar study on borophene supercapacitors.[23] We initially started our study with CANDLE, but after analyzing around 2,500 materials, we observed that for a lot of cases, CANDLE is producing a somewhat unphysical discontinuity in the *V*-*Q* curve that has also been reported for a tricky case before.[21] Our benchmarking tests reveal that SaLSA produces a reasonable capacitive response in most of these cases. As an example, we show the case of H_2O_2S-b_AB2C2-12-ci (Figure S8; Table S4), where most of the LinearPCM and Nonlinear-PCM models produce a nonlinear or even a discontinuous response, but SaLSA produces a perfectly linear *V*-*Q* curve with near-zero residual error. As a result, we decided not to compromise with the accuracy of the obtained results and adopt the costlier but fully non-empirical SaLSA model for all calculations.

H_2O has been used as the choice of solvent, as aqueous-medium-based supercapacitor studies are the most common.[11,12,23] However, our benchmarking tests (Figure S13; Table S7) reveal that the effect of solvent is minimal on the capacitive response or the specific capacitance, but can affect the PZC significantly. This is expected as the organic solvents usually offer a higher electrochemical voltage window than water. Therefore, the specific capacitances predicted in our study should be transferable to other solvents, albeit the PZC would not.

Most materials have been virtually immersed in a 12 Å thick electrolyte layer for simulating the capacitive response. For some unusually thick 2D materials, JDFTx fails with this setting, and a slightly thicker layer of 14 Å had to be used.

The ionic strength of the electrolyte has been taken as 6 M, following the previous standards.[23] Our benchmarking tests (Figure S15) show that except for the very dilute limit (0.01 M), the ionic strength barely affects the PZC or the capacitive response, again making our specific capacitance and even the PZC predictions very universal.

Unlike LinearPCM and Nonlinear-PCM models, the choice of conducting ions in the SaLSA model can affect the capacitive response.[15] Conforming to the previous

standards (http://jdftx.org/SolvationIon.html),[23] we use the Na^+ and F^- ions to predict the non-absorbing capacitive responses of the materials. However, our benchmarking tests (Figure S16; Table S9) show that the type of cation does not have any effect on the PZC or the capacitive response, whereas the type of anion can slightly affect the capacitive response but significantly alter the PZC.

We make an informed choice of using non-spin-polarized calculations throughout, without any empirical Hubbard-*U* corrections. The non-spin-polarized calculations are almost 1.5–2 times faster than the spin-polarized calculations. Also, determining the magnetic ground state of materials can be a very involved process.[37] Furthermore, while some DFT codes do allow to determine the value of the parameter *U* using a linear-response method (which is also a very extensive process),[93] JDFTx lacks this functionality. Using *U* values from the literature is also not possible as most of the explored materials in this work have never been exposed to such studies, and these values are also highly pseudopotential dependent and therefore not transferable. To understand the effect of this choice on the capacitive properties, we choose two famous 2D FM materials, CrI_3 and $Cr_2Ge_2Te_6$, as the ideal candidates for benchmarking.[94,95] The Materials Project (https://docs.materialsproject.org/methodology/gga-plus-u) determines the effective *U* value of Cr as 3.7 eV, where these effective *U* values have been calibrated by performing a fitting to experimental binary formation enthalpies.[96] Although this value is intended for a different DFT code and is heavily pseudopotential dependent, it gives us an idea about the range of *U* values we may try. We use $U = [0, 1, 2, 3, 4, 5, 6, 7]$ eV for both materials as our benchmarking test and document their capacitive properties as shown in Figures S10 and S11. For both cases, the introduction of *U* makes the *V*-*Q* curve highly jagged and slightly nonlinear. For $Cr_2Ge_2Te_6$, $U = 7.0$ eV produces an unphysical all-positive surface charge, even with negative applied voltage. Although the PZC changes significantly with different *U* values, the change in the specific capacitance appears minimal. The jagged nature of the curves also introduces huge residual error for the linear fitting processes; therefore, a slight variation of the specific capacitance is expected anyway. However, the non-magnetic (NM) and the ferromagnetic (FM) solution with $U = 0$ produce very close capacitive properties, including the PZC. These results justify our choice of using non-spin-polarized calculations for this high-throughput study.

All calculations have been performed using applied voltage $V \in [-0.6, 0.6]$ V with an interval of 0.2 V. However, for all focused benchmarking studies mentioned above, this interval has been reduced to 0.1 V to get a smoother response and a better fit. As a result, for the former case a 7-points fitting and for the latter a 13-points fitting is performed to obtain the capacitance. Therefore, the specific capacitance (slightly) and residual error (significantly) values may vary from the high-throughput calculations to the benchmarking tests.

Automated high-throughput computation methodology

For the high-throughput methodologies developed for this work, the Python library pymatgen (Python Materials Genomics)[97] has been used extensively. The library Atomic Simulation Environment (ASE)[98] has also been used for some operations. Especially, the adsorption module[49] from pymatgen is crucial to this work for finding the possible Li-binding sites in an automated manner. Suitably modified versions of MPRelaxSet and MPStaticSet from pymatgen.io.vasp.sets have been used to perform the structural relaxations and the static runs. After these calculations finish, the symm_reduce function from the adsorption module has been used to detect equivalent adsorption sites, which takes a threshold value as an input. However,

due to the Li-ion adsorption induced structural changes, it is next to impossible to determine a "one-size-fits-all" threshold value that would be suitable for all the adsorbed structures. Sometimes the structural changes are so severe that the function completely fails to determine the symmetry. After rigorous testing, we define a threshold of 0.175 for all materials. However, this value still fails to perform proper symmetry reduction for some structures. With this threshold value, the algorithm does correctly identify the correct number of unique adsorption sites for symmetric MoS_2 and asymmetric ReS_2.

Nevertheless, this number is not an essential quantity for our analysis as we are only interested in the most stable binding site, which is favored at full-capacity adsorption.

ML

For the ML part, both Crystal Graph Convolutional Neural Networks (CGCNN)[63] and MEGNet[64,65] have been tested. We have added a total of 30 Å (15 Å on each side) vacuum to all structures to ensure that the graph network does not add spurious neighbors in the vertical direction from periodically adjacent cells. To perform a fair comparison, the data were divided into random train and test sets, with a ratio of 0.8:0.2. The best model was chosen based on the models' performance on the 20% test data. Parameters such as the maximum number of neighbors and cutoff radius for building the crystal graphs are varied, and the performance of the models is checked on the test set. The best MEGNet model outperforms the best CGCNN model, and thus the MEGNet framework has been chosen for further training. For the supercapacitance prediction, the models are trained to predict the average integral capacitance, an intrinsic property of the material. The specific area can be obtained from the crystal structure itself; subsequently, the specific capacitance can be estimated. While searching other databases, the ML model sees unoptimized structures (optimized using other DFT codes and parameters), and the integral capacitance, specific area, and ultimately the specific capacitance are predicted based on this unoptimized lattice. We have observed that the specific capacitance estimated with the unoptimized structure and the optimized structure is very close for most materials except for a select few, where the surface area changes significantly after lattice optimization by JDFTx.

SUPPLEMENTAL INFORMATION

Supplemental information can be found online at https://doi.org/10.1016/j.xcrp.2021.100718.

ACKNOWLEDGMENTS

This work was supported by the Material for Energy Storage (MES) scheme of Technology Mission Division Energy and Water, Department of Science and Technology (DST), Government of India, under grant DST/TMD/MES/2K18/28. The authors thank Dr. Biswapriyo Das for his help in graphical abstract creation.

AUTHOR CONTRIBUTIONS

A.K. developed the high-throughput automated methodologies and codes, performed the (J)DFT calculations, implemented the ML models, and analyzed the results. S.M. conceived the problem statement and supervised the overall work. Both authors contributed to the writing.

DECLARATION OF INTERESTS

The authors declare no competing interests.

Received: October 13, 2021
Revised: November 29, 2021
Accepted: December 13, 2021
Published: January 10, 2022

REFERENCES

1. Sun, X., Li, Z., Wang, X., and Li, C. (2020). Technology Development of Electric Vehicles: A Review. Energies *13*, 90.

2. Miao, Y., Hynan, P., von Jouanne, A., and Yokochi, A. (2019). Current Li-Ion Battery Technologies in Electric Vehicles and Opportunities for Advancements. Energies *12*, 1074.

3. Huang, S., Zhu, X., Sarkar, S., and Zhao, Y. (2019). Challenges and opportunities for supercapacitors. APL Mater. *7*, 100901.

4. Novoselov, K.S., Geim, A.K., Morozov, S.V., Jiang, D., Zhang, Y., Dubonos, S.V., Grigorieva, I.V., and Firsov, A.A. (2004). Electric field effect in atomically thin carbon films. Science *306*, 666–669.

5. Hynek, D.J., Pondick, J.V., and Cha, J.J. (2019). The development of 2D materials for electrochemical energy applications: A mechanistic approach. APL Mater. *7*, 30902.

6. Mujib, S.B., Ren, Z., Mukherjee, S., Soares, D.M., and Singh, G. (2020). Design, characterization, and application of elemental 2D materials for electrochemical energy storage, sensing, and catalysis. Mater. Adv. *1*, 2562–2591.

7. Zhai, S., Wei, L., Karahan, H.E., Chen, X., Wang, C., Zhang, X., Chen, J., Wang, X., and Chen, Y. (2019). 2D materials for 1D electrochemical energy storage devices. Energy Storage Mater. *19*, 102–123.

8. Chen, K.-S., Balla, I., Luu, N.S., and Hersam, M.C. (2017). Emerging Opportunities for Two-Dimensional Materials in Lithium-Ion Batteries. ACS Energy Lett. *2*, 2026–2034.

9. Shi, L., and Zhao, T. (2017). Recent advances in inorganic 2D materials and their applications in lithium and sodium batteries. J. Mater. Chem. A Mater. Energy Sustain. *5*, 3735–3758.

10. Bahari, Y., Mortazavi, B., Rajabpour, A., Zhuang, X., and Rabczuk, T. (2021). Application of two-dimensional materials as anodes for rechargeable metal-ion batteries: A comprehensive perspective from density functional theory simulations. Energy Storage Mater. *35*, 203–282.

11. Kumar, K.S., Choudhary, N., Jung, Y., and Thomas, J. (2018). Recent Advances in Two-Dimensional Nanomaterials for Supercapacitor Electrode Applications. ACS Energy Lett. *3*, 482–495.

12. Raj, B., Padhy, A.K., Basu, S., and Mohapatra, M. (2020). Review—Futuristic Direction for R&D Challenges to Develop 2D Advanced Materials Based Supercapacitors. J. Electrochem. Soc. *167*, 136501.

13. Petrosyan, S.A., Rigos, A.A., and Arias, T.A. (2005). Joint density-functional theory: ab initio study of Cr2O3 surface chemistry in solution. J. Phys. Chem. B *109*, 15436–15444.

14. Sundararaman, R., Goddard, W.A., 3rd, and Arias, T.A. (2017). Grand canonical electronic density-functional theory: Algorithms and applications to electrochemistry. J. Chem. Phys. *146*, 114104.

15. Sundararaman, R., Schwarz, K.A., Letchworth-Weaver, K., and Arias, T.A. (2015). Spicing up continuum solvation models with SaLSA: the spherically averaged liquid susceptibility ansatz. J. Chem. Phys. *142*, 054102.

16. Sundararaman, R., and Goddard, W.A., 3rd (2015). The charge-asymmetric nonlocally determined local-electric (CANDLE) solvation model. J. Chem. Phys. *142*, 064107.

17. Sundararaman, R., Gunceler, D., and Arias, T.A. (2014). Weighted-density functionals for cavity formation and dispersion energies in continuum solvation models. J. Chem. Phys. *141*, 134105.

18. Sundararaman, R., Letchworth-Weaver, K., and Arias, T.A. (2012). A computationally efficacious free-energy functional for studies of inhomogeneous liquid water. J. Chem. Phys. *137*, 044107.

19. Sundararaman, R., and Arias, T.A. (2014). Efficient classical density-functional theories of rigid-molecular fluids and a simplified free energy functional for liquid water. Comput. Phys. Commun. *185*, 818–825.

20. Sundararaman, R., and Schwarz, K. (2017). Evaluating continuum solvation models for the electrode-electrolyte interface: Challenges and strategies for improvement. J. Chem. Phys. *146*, 084111.

21. Sundararaman, R., Letchworth-Weaver, K., and Schwarz, K.A. (2018). Improving accuracy of electrochemical capacitance and solvation energetics in first-principles calculations. J. Chem. Phys. *148*, 144105.

22. Sundararaman, R., Letchworth-Weaver, K., Schwarz, K.A., Gunceler, D., Ozhabes, Y., and Arias, T.A. (2017). JDFTx: software for joint density-functional theory. SoftwareX *6*, 278–284.

23. Zhan, C., Zhang, P., Dai, S., and Jiang, D.E. (2016). Boron Supercapacitors. ACS Energy Lett. *1*, 1241–1246.

24. Stoller, M.D., Park, S., Zhu, Y., An, J., and Ruoff, R.S. (2008). Graphene-based ultracapacitors. Nano Lett. *8*, 3498–3502.

25. Ji, H., Zhao, X., Qiao, Z., Jung, J., Zhu, Y., Lu, Y., Zhang, L.L., MacDonald, A.H., and Ruoff, R.S. (2014). Capacitance of carbon-based electrical double-layer capacitors. Nat. Commun. *5*, 3317.

26. Putungan, D.B., Lin, S.H., and Kuo, J.L. (2016). Metallic VS2 Monolayer Polytypes as Potential Sodium-Ion Battery Anode via ab Initio Random Structure Searching. ACS Appl. Mater. Interfaces *8*, 18754–18762.

27. George, C., Morris, A.J., Modarres, M.H., and De Volder, M. (2016). Structural Evolution of Electrochemically Lithiated MoS_2 Nanosheets and the Role of Carbon Additive in Li-Ion Batteries. Chem. Mater. *28*, 7304–7310.

28. Kabiraj, A., and Mahapatra, S. (2018). High-throughput first-principles-calculations based estimation of lithium ion storage in monolayer rhenium disulfide. Commun. Chem. *1*, 81.

29. Mounet, N., Gibertini, M., Schwaller, P., Campi, D., Merkys, A., Marrazzo, A., Sohier, T., Castelli, I.E., Cepellotti, A., Pizzi, G., and Marzari, N. (2018). Two-dimensional materials from high-throughput computational exfoliation of experimentally known compounds. Nat. Nanotechnol. *13*, 246–252.

30. Rajan, A.C., Mishra, A., Satsangi, S., Vaish, R., Mizuseki, H., Lee, K.-R., and Singh, A.K. (2018). Machine-Learning-Assisted Accurate Band Gap Predictions of Functionalized MXene. Chem. Mater. *30*, 4031–4038.

31. Choudhary, K., Kalish, I., Beams, R., and Tavazza, F. (2017). High-throughput Identification and Characterization of Two-dimensional Materials using Density functional theory. Sci. Rep. *7*, 5179.

32. Choudhary, K., Garrity, K.F., Reid, A.C.E., DeCost, B., Biacchi, A.J., Hight Walker, A.R., Trautt, Z., Hattrick-Simpers, J., Kusne, A.G., Centrone, A., et al. (2020). The joint automated repository for various integrated simulations (JARVIS) for data-driven materials design. npj Comput. Mater. *6*, 173.

33. Zhou, J., Shen, L., Costa, M.D., Persson, K.A., Ong, S.P., Huck, P., Lu, Y., Ma, X., Chen, Y., Tang, H., and Feng, Y.P. (2019). 2DMatPedia, an open computational database of two-dimensional materials from top-down and bottom-up approaches. Sci. Data *6*, 86.

34. Haastrup, S., Strange, M., Pandey, M., Deilmann, T., Schmidt, P.S., Hinsche, N.F., Gjerding, M.N., Torelli, D., Larsen, P.M., Riis-Jensen, A.C., et al. (2018). The Computational

2D Materials Database: high-throughput modeling and discovery of atomically thin crystals. 2D Mater. *5*, 42002.

35. Gjerding, M.N., Taghizadeh, A., Rasmussen, A., Ali, S., Bertoldo, F., Deilmann, T., Holguin, U.P., Knøsgaard, N.R., Kruse, M., Manti, S., et al. (2021). Recent Progress of the Computational 2D Materials Database (C2DB). 2D Mater. *8*, 044002.

36. Marrazzo, A., Gibertini, M., Campi, D., Mounet, N., and Marzari, N. (2019). Relative Abundance of [Formula: see text] Topological Order in Exfoliable Two-Dimensional Insulators. Nano Lett. *19*, 8431–8440.

37. Kabiraj, A., Kumar, M., and Mahapatra, S. (2020). High-throughput discovery of high Curie point two-dimensional ferromagnetic materials. npj Comput. Mater. *6*, 35.

38. Karmodak, N., and Andreussi, O. (2020). Catalytic Activity and Stability of Two-Dimensional Materials for the Hydrogen Evolution Reaction. ACS Energy Lett. *5*, 885–891.

39. Zhang, X., Zhang, Z., Wu, D., Zhang, X., Zhao, X., and Zhou, Z. (2018). Computational Screening of 2D Materials and Rational Design of Heterojunctions for Water Splitting Photocatalysts. Small Methods *2*, 1700359.

40. Kabiraj, A., and Mahapatra, S. (2020). Machine-Intelligence-Driven High-Throughput Prediction of 2D Charge Density Wave Phases. J. Phys. Chem. Lett. *11*, 6291–6298.

41. Sreepal, V., Yagmurcukardes, M., Vasu, K.S., Kelly, D.J., Taylor, S.F.R., Kravets, V.G., Kudrynskyi, Z., Kovalyuk, Z.D., Patanè, A., Grigorenko, A.N., et al. (2019). Two-Dimensional Covalent Crystals by Chemical Conversion of Thin van der Waals Materials. Nano Lett. *19*, 6475–6481.

42. Han, M., Maleski, K., Shuck, C.E., Yang, Y., Glazar, J.T., Foucher, A.C., Hantanasirisakul, K., Sarycheva, A., Frey, N.C., May, S.J., et al. (2020). Tailoring Electronic and Optical Properties of MXenes through Forming Solid Solutions. J. Am. Chem. Soc. *142*, 19110–19118.

43. Wang, L., Han, M., Shuck, C.E., Wang, X., and Gogotsi, Y. (2021). Adjustable electrochemical properties of solid-solution MXenes. Nano Energy *88*, 106308.

44. Urban, A., Seo, D.-H., and Ceder, G. (2016). Computational understanding of Li-ion batteries. npj Comput. Mater. *2*, 16002.

45. Tang, Q., Zhou, Z., and Shen, P. (2012). Are MXenes promising anode materials for Li ion batteries? Computational studies on electronic properties and Li storage capability of Ti3C2 and Ti3C2X2 (X = F, OH) monolayer. J. Am. Chem. Soc. *134*, 16909–16916.

46. He, Q., Yu, B., Li, Z., and Zhao, Y. (2019). Density Functional Theory for Battery Materials. Energy Environ. Mater. *2*, 264–279.

47. Kabiraj, A., Bhattacharyya, A.J., and Mahapatra, S. (2021). Thermodynamic Insights into Polymorphism-Driven Lithium-Ion Storage in Monoelemental 2D Materials. J. Phys. Chem. Lett. *12*, 1220–1227.

48. Kabiraj, A., and Mahapatra, S. (2020). Intercalation-Driven Reversible Switching of 2D Magnetism. J. Phys. Chem. C *124*, 1146–1157.

49. Montoya, J.H., and Persson, K.A. (2017). A high-throughput framework for determining adsorption energies on solid surfaces. npj Comput. Mater. *3*, 14.

50. Jiang, H.R., Shyy, W., Liu, M., Wei, L., Wu, M.C., and Zhao, T.S. (2017). Boron phosphide monolayer as a potential anode material for alkali metal-based batteries. J. Mater. Chem. A Mater. Energy Sustain. *5*, 672–679.

51. Tao, L., Cinquanta, E., Chiappe, D., Grazianetti, C., Fanciulli, M., Dubey, M., Molle, A., and Akinwande, D. (2015). Silicene field-effect transistors operating at room temperature. Nat. Nanotechnol. *10*, 227–231.

52. Saha, D., and Mahapatra, S. (2016). Atomistic modeling of the metallic-to-semiconducting phase boundaries in monolayer MoS2. Appl. Phys. Lett. *108*, 253106.

53. Kappera, R., Voiry, D., Yalcin, S.E., Branch, B., Gupta, G., Mohite, A.D., and Chhowalla, M. (2014). Phase-engineered low-resistance contacts for ultrathin MoS2 transistors. Nat. Mater. *13*, 1128–1134.

54. Zhang, Q., Tan, S., Mendes, R.G., Sun, Z., Chen, Y., Kong, X., Xue, Y., Rümmeli, M.H., Wu, X., Chen, S., and Fu, L. (2016). Extremely Weak van der Waals Coupling in Vertical ReS2 Nanowalls for High-Current-Density Lithium-Ion Batteries. Adv. Mater. *28*, 2616–2623.

55. Samad, A., and Schwingenschlögl, U. (2021). M_2X Monolayers as Anode Materials for Li Ion Batteries. Phys. Rev. Appl. *15*, 34025.

56. Lv, X., Wei, W., Sun, Q., Yu, L., Huang, B., and Dai, Y. (2017). Sc_2 C as a Promising Anode Material with High Mobility and Capacity: A First-Principles Study. ChemPhysChem *18*, 1627–1634.

57. Zhao, S., Kang, W., and Xue, J. (2014). Role of Strain and Concentration on the Li Adsorption and Diffusion Properties on Ti2C Layer. J. Phys. Chem. C *118*, 14983–14990.

58. Kurahashi, S., Arabnejad, S., Ushiyama, H., and Yamashita, K. (2019). Li and Na Interaction with Ti_2C-MXene: A First-Principles Calculation. J. Comput. Chem. Jpn. *18*, 84–94.

59. Wang, D., Gao, Y., Liu, Y., Jin, D., Gogotsi, Y., Meng, X., Du, F., Chen, G., and Wei, Y. (2017). First-Principles Calculations of Ti2N and Ti2NT2 (T = O, F, OH) Monolayers as Potential Anode Materials for Lithium-Ion Batteries and Beyond. J. Phys. Chem. C *121*, 13025–13034.

60. Schmidt, J., Marques, M.R.G., Botti, S., and Marques, M.A.L. (2019). Recent advances and applications of machine learning in solid-state materials science. npj Comput. Mater. *5*, 83.

61. Chen, A., Zhang, X., and Zhou, Z. (2020). Machine learning: Accelerating materials development for energy storage and conversion. InfoMat *2*, 553–576.

62. Song, Y., Siriwardane, E.M.D., Zhao, Y., and Hu, J. (2021). Computational Discovery of New 2D Materials Using Deep Learning Generative Models. ACS Appl. Mater. Interfaces *13*, 53303–53313.

63. Xie, T., and Grossman, J.C. (2018). Crystal Graph Convolutional Neural Networks for an Accurate and Interpretable Prediction of Material Properties. Phys. Rev. Lett. *120*, 145301.

64. Chen, C., Ye, W., Zuo, Y., Zheng, C., and Ong, S.P. (2019). Graph Networks as a Universal Machine Learning Framework for Molecules and Crystals. Chem. Mater. *31*, 3564–3572.

65. Chen, C., Zuo, Y., Ye, W., Li, X., and Ong, S.P. (2021). Learning properties of ordered and disordered materials from multi-fidelity data. Nat. Comput. Sci. *1*, 46–53.

66. Dunn, A., Wang, Q., Ganose, A., Dopp, D., and Jain, A. (2020). Benchmarking materials property prediction methods: the Matbench test set and Automatminer reference algorithm. npj Comput. Mater. *6*, 138.

67. Xiong, Z., Cui, Y., Liu, Z., Zhao, Y., Hu, M., and Hu, J. (2020). Evaluating explorative prediction power of machine learning algorithms for materials discovery using k-fold forward cross-validation. Comput. Mater. Sci. *171*, 109203.

68. Pickard, C.J., and Needs, R.J. (2011). Ab initio random structure searching. J. Phys. Condens. Matter *23*, 053201.

69. Papadopoulou, K.A., Chroneos, A., Parfitt, D., and Christopoulos, S.-R.G. (2020). A perspective on MXenes: Their synthesis, properties, and recent applications. J. Appl. Physiol. *128*, 170902.

70. Ibragimova, R., Erhart, P., Rinke, P., and Komsa, H.-P. (2021). Surface Functionalization of 2D MXenes: Trends in Distribution, Composition, and Electronic Properties. J. Phys. Chem. Lett. *12*, 2377–2384.

71. Li, Q., Kolluru, V.S.C., Rahn, M.S., Schwenker, E., Li, S., Hennig, R.G., Darancet, P., Chan, M.K.Y., and Hersam, M.C. (2021). Synthesis of borophane polymorphs through hydrogenation of borophene. Science *371*, 1143–1148.

72. Li, J., Tritsaris, G.A., Zhang, X., Shi, B., Yang, C., Liu, S., Yang, J., Xu, L., Yang, J., Pan, F., et al. (2020). Monolayer Honeycomb Borophene: A Promising Anode Material with a Record Capacity for Lithium-Ion and Sodium-Ion Batteries. J. Electrochem. Soc. *167*, 090527.

73. Li, W., Kong, L., Chen, C., Gou, J., Sheng, S., Zhang, W., Li, H., Chen, L., Cheng, P., and Wu, K. (2018). Experimental realization of honeycomb borophene. Sci. Bull. (Beijing) *63*, 282–286.

74. Ryou, J., Kim, Y.-S., Kc, S., and Cho, K. (2016). Monolayer MoS2 Bandgap Modulation by Dielectric Environments and Tunable Bandgap Transistors. Sci. Rep. *6*, 29184.

75. Soon, J.M., and Loh, K.P. (2007). Electrochemical Double-Layer Capacitance of MoS_2 Nanowall Films. Electrochem. Solid-State Lett. *10*, A250.

76. Valette, G. (1982). Double layer on silver single crystal electrodes in contact with electrolytes having anions which are slightly specifically adsorbed: Part II. The (100) face. J. Electroanal. Chem. Interfacial Electrochem. *138*, 37–54.

77. Mannix, A.J., Zhou, X.-F., Kiraly, B., Wood, J.D., Alducin, D., Myers, B.D., Liu, X., Fisher, B.L.,

Santiago, U., Guest, J.R., et al. (2015). Synthesis of borophenes: Anisotropic, two-dimensional boron polymorphs. Science *350*, 1513–1516.

78. Feng, B., Zhang, J., Zhong, Q., Li, W., Li, S., Li, H., Cheng, P., Meng, S., Chen, L., and Wu, K. (2016). Experimental realization of two-dimensional boron sheets. Nat. Chem. *8*, 563–568.

79. Abdolhosseini, S., Boroun, M., and Pourfath, M. (2021). Ab Initio Analysis of Periodic Self-Assembly Phases of Borophene as Anode Material for Na-Ion Batteries. J. Phys. Chem. C *125*, 5436–5446.

80. Kresse, G., and Hafner, J. (1993). Ab initio molecular dynamics for liquid metals. Phys. Rev. B Condens. Matter *47*, 558–561.

81. Kresse, G., and Hafner, J. (1994). Ab initio molecular-dynamics simulation of the liquid-metal-amorphous-semiconductor transition in germanium. Phys. Rev. B Condens. Matter *49*, 14251–14269.

82. Kresse, G., and Furthmüller, J. (1996). Efficient iterative schemes for ab initio total-energy calculations using a plane-wave basis set. Phys. Rev. B Condens. Matter *54*, 11169–11186.

83. Kresse, G., and Furthmüller, J. (1996). Efficiency of ab-initio total energy calculations for metals and semiconductors using a plane-wave basis set. Comput. Mater. Sci. *6*, 15–50.

84. Kresse, G., and Joubert, D. (1999). From ultrasoft pseudopotentials to the projector augmented-wave method. Phys. Rev. B Condens. Matter Mater. Phys. *59*, 1758–1775.

85. Perdew, J.P., Burke, K., and Ernzerhof, M. (1996). Generalized Gradient Approximation Made Simple. Phys. Rev. Lett. *77*, 3865–3868.

86. Grimme, S., Antony, J., Ehrlich, S., and Krieg, H. (2010). A consistent and accurate ab initio parametrization of density functional dispersion correction (DFT-D) for the 94 elements H-Pu. J. Chem. Phys. *132*, 154104.

87. Momma, K., and Izumi, F. (2011). VESTA 3 for three-dimensional visualization of crystal, volumetric and morphology data. J. Appl. Cryst. *44*, 1272–1276.

88. Schlipf, M., and Gygi, F. (2015). Optimization algorithm for the generation of ONCV pseudopotentials. Comput. Phys. Commun. *196*, 36–44.

89. Garrity, K.F., Bennett, J.W., Rabe, K.M., and Vanderbilt, D. (2014). Pseudopotentials for high-throughput DFT calculations. Comput. Mater. Sci. *81*, 446–452.

90. Gunceler, D., Letchworth-Weaver, K., Sundararaman, R., Schwarz, K.A., and Arias, T.A. (2013). The importance of nonlinear fluid response in joint density-functional theory studies of battery systems. Model. Simul. Mater. Sci. Eng. *21*, 74005.

91. Andreussi, O., Dabo, I., and Marzari, N. (2012). Revised self-consistent continuum solvation in electronic-structure calculations. J. Chem. Phys. *136*, 064102.

92. Fisicaro, G., Genovese, L., Andreussi, O., Mandal, S., Nair, N.N., Marzari, N., and Goedecker, S. (2017). Soft-Sphere Continuum Solvation in Electronic-Structure Calculations. J. Chem. Theory Comput. *13*, 3829–3845.

93. Cococcioni, M., and de Gironcoli, S. (2005). Linear response approach to the calculation of the effective interaction parameters in the LDA+U method. Phys. Rev. B Condens. Matter Mater. Phys. *71*, 35105.

94. Huang, B., Clark, G., Navarro-Moratalla, E., Klein, D.R., Cheng, R., Seyler, K.L., Zhong, D., Schmidgall, E., McGuire, M.A., Cobden, D.H., et al. (2017). Layer-dependent ferromagnetism in a van der Waals crystal down to the monolayer limit. Nature *546*, 270–273.

95. Gong, C., Li, L., Li, Z., Ji, H., Stern, A., Xia, Y., Cao, T., Bao, W., Wang, C., Wang, Y., et al. (2017). Discovery of intrinsic ferromagnetism in two-dimensional van der Waals crystals. Nature *546*, 265–269.

96. Wang, L., Maxisch, T., and Ceder, G. (2006). Oxidation energies of transition metal oxides within the GGA+U framework. Phys. Rev. B Condens. Matter Mater. Phys. *73*, 195107.

97. Ong, S.P., Richards, W.D., Jain, A., Hautier, G., Kocher, M., Cholia, S., Gunter, D., Chevrier, V.L., Persson, K.A., and Ceder, G. (2013). Python Materials Genomics (pymatgen): A robust, open-source python library for materials analysis. Comput. Mater. Sci. *68*, 314–319.

98. Hjorth Larsen, A., Jørgen Mortensen, J., Blomqvist, J., Castelli, I.E., Christensen, R., Dułak, M., Friis, J., Groves, M.N., Hammer, B., Hargus, C., et al. (2017). The atomic simulation environment-a Python library for working with atoms. J. Phys. Condens. Matter *29*, 273002.